國 立 交 通 大 學

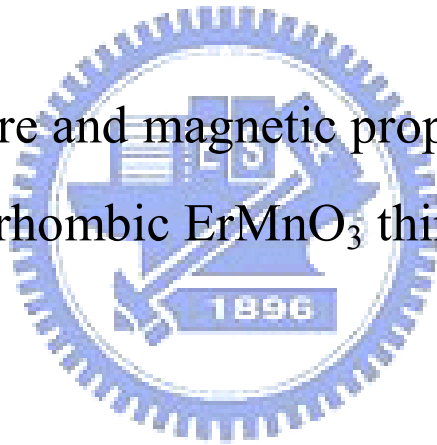## 電子物理系

碩士論文

正交結構鉺錳氧薄膜之結構與磁
各向異性研究

Structure and magnetic properties in

orthorhombic ErMnO$_3$ thin films

研究生：張凱婷

指導教授：莊振益 教授

中華民國九十八年七月

正交結構鉺錳氧薄膜之結構與磁各向異性研究

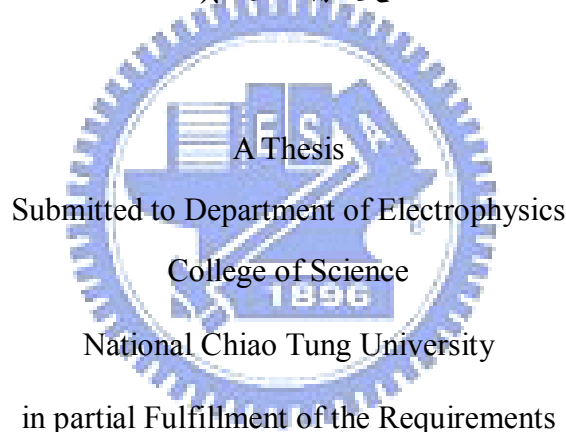# Structure and magnetic properties in orthorhombic ErMnO$_3$ thin films

研 究 生：張凱婷   Student：Kai-Ting Chang

指導教授：莊振益   Advisor：Prof. Jenh-Yih Juang

國 立 交 通 大 學

電 子 物 理 學 系

碩 士 論 文

A Thesis

Submitted to Department of Electrophysics

College of Science

National Chiao Tung University

in partial Fulfillment of the Requirements

for the Degree of

Master

in

Electrophysics

July 2009

Hsinchu, Taiwan, Republic of China

中 華 民 國 九 十 八 年 七 月

正交結構鉺錳氧薄膜之結構與磁各向異性研究

研究生：張凱婷　　　　　　　　　　　　　指導教授：莊振益 教授

國立交通大學　電子物理學系碩士班

中文摘要

本研究選用鑭鋁氧(110)與鈦酸鍶(100)兩種基板，利用雷射濺鍍分別製備b軸與c軸垂直基板的正交結構鉺錳氧薄膜，並研究其結構與磁特性。我們發現三個磁性轉折點，第一個轉折點發生於42K為尼爾溫度，是由錳的反鐵磁磁序引起的；第二轉折點可能為錳的自旋重新排列所導致的，成長於兩種基板上的鉺錳氧其第二個轉折溫度有很大的不同；最後一個出現在低溫的轉折係因稀土元素鉺所引發的。其中，尼爾溫度和鉺的轉折不會因成長的基板而有所不同，然而錳的自旋重新排列轉折在不同的基板上卻有10K的差距，這可能是由於成長於不同基板上取向附生的應力所造成的差異。此外我們也針對低氧壓環境下製備薄膜會造成的影響做了討論。

Structure and magnetic properties in orthorhombic ErMnO$_3$ thin films

Student: Kai-Ting Chang   Advisor: Prof. Jenh-Yih Juang

Department of Electrophysics

National Chiao Tung University

Abstract

We have investigated the structure and magnetic properties of b and c-axis-oriented multiferroic orthorhombic ErMnO$_3$ (o-ErMO) films deposited on LaAlO$_3$(110) and SrTiO$_3$(001) substrate, respectively, by pulsed laser deposition. Three distinctive magnetic transitions were observed for o-ErMO films grown on both LAO and STO substrates. The first one locating around 42K is apparently associated to the antiferromagnetic ordering of Mn moment and, thus, it is assigned as the Neel temperature (T_N). The second transition was observed near 18K for o-ErMO/LAO(110), which is markedly different from the transition at 28K for o-ErMO/STO(001). The last transition was dominated by the moments from erbium ions at lower temperatures. The two AFM transitions of Mn^{3+} and Er^{3+} moments appear to be rather insensitive to the substrates on which the films were grown. However, there is a 10-Kelvin difference in the spin reorientation transition identified for the Mn-moment when

different substrates were used. This discrepancy seems to be more relevant to the strain arising from film/substrate epitaxy. Besides, in order to clarify the effect of low oxygen partial pressures on the magnetic structure, we also compare the structure and magnetic properties of the o-ErMO films prepared under very different oxygen partial pressures.

Acknowledgement

Table of Contents

List of Tables

List of Figures

Chap.1 Introduction

1.1. Background

Multiferroics are materials displaying the coexistence of ordered magnetism and ferroelectricity. One interesting characteristic of these materials is that the electric properties can be controlled by applied magnetic field and vice versa [1-3]. In general, since the different requirements of ferroelectricity and magnetism in filling of their d shells make these two ordered states often mutually exclusive, few materials exhibit mutltiferroics [4]. Cheong *et al.* has summarized and classified materials into "proper" or "improper" ferroelectrics according to the mechanism resulting in ferroelectricity [5]. The proper ferroelectrics result from the structural instability toward the polar state associated with the electric pairing. On the other hand, the ferroelectricity whose polarization is caused by a complex distortion or an accidental by-product of some other ordering is called "improper". Among these, orthorhombic $RMnO_3$, whose polarization is induced by magnetic orderings and hence strong couplings between magnetism and ferroelectricity is expected, is the front runner candidate for potentially useful applications within these multiferroicities. Therefore, understanding the coupling between the magnetism and ferroelectricity and sketching various kinds of potential novel applications using multiferroic $RMnO_3$ have evoked tremendous research interest recently [1, 5-8].

Table 1.1 Classification of ferroelectrics [5]

Classification of ferroelectrics		
	Mechanism of inversion symmetry Breaking	Materials
Proper	Covalent bonding between $3d^0$ transition metal (Ti) and oxygen	$BaTiO_3$
	Polarization of $6s^2$ lone pair of Bi or Pb	$BiMnO_3$, $BiFeO_3$, $Pb(Fe_{2/3}W_{1/3})O_3$
Improper	Structural transition *'Geometric ferroelectrics'*	K_2SeO_4, Cs_2CdI_4 hexagonal $RMnO_3$
	Charge ordering *'Electronic ferroelectrics'*	$LuFe_2O_4$
	Magnetic ordering *'Magnetic ferroelectrics'*	**Orthorhombic $RMnO_3$** RMn_2O_5, $CoCr_2O$

The $RMnO_3$ system is structurally divided into a couple of subsystems. As shown in Fig 1.1 [9], the $RMnO_3$ with larger rare earths, R=La-Dy, have stable orthorhombic structure in *pbnm* space group, whereas the $RMnO_3$ with smaller rare earths, R=Sc, Y and Ho-Lu, have stable hexagonal structure in *p6₃cm* space group. Nonetheless, metastable orthorhombic perovskites of smaller rare earths can possibly be prepared by means of high temperature, high pressure process [10, 11], soft chemistry procedures [12, 13] as well as being prepared in form of thin films that are stabilized by epitaxial strain from the substrate [6-8]. These methods of manipulating the desired structure transition in $RMnO_3$ provide a chance to search for more materials with potentially stronger couplings between magnetism and ferroelectricity.
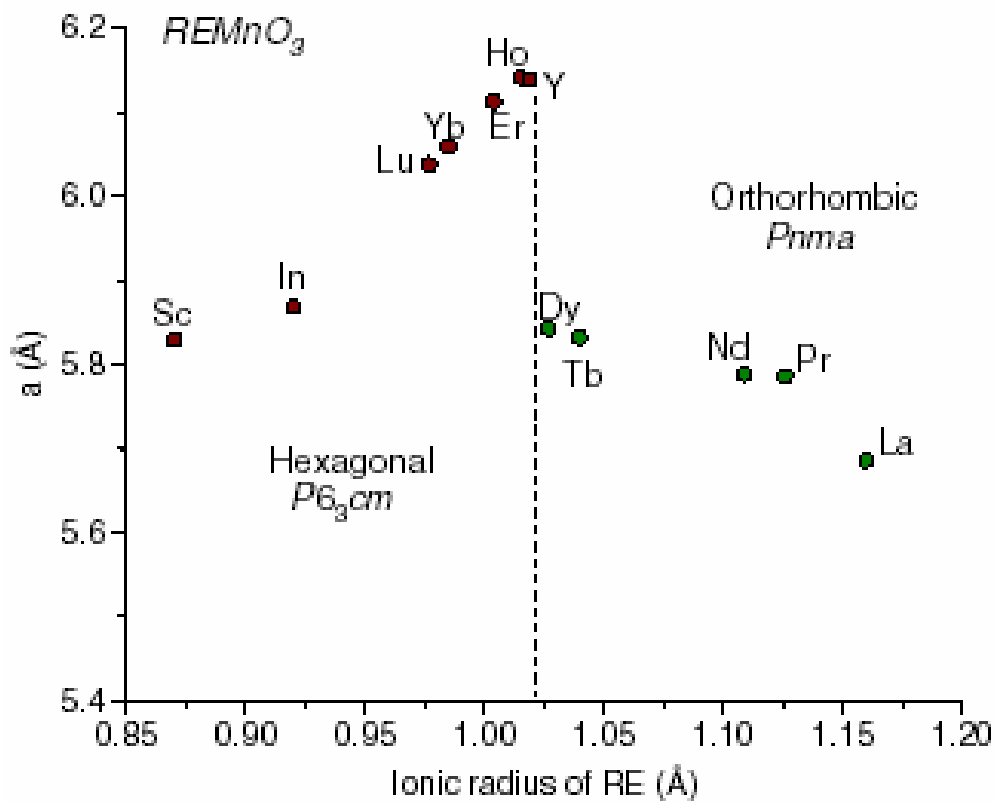
Fig. 1.1 Evolution of the lattice structure in REMnO₃ as a function of the size of the rare earth (RE).

Within RMnO₃ family, TbMnO₃ and DyMnO₃ indeed have been demonstrated to exhibit a rather weak magnetism-induced polarization ($P=0.1\mu C/cm^2$) due to the weak coupling between non-collinear magnetic phase and ferroelectricity [1, 14]. In these cases, the primary physical mechanism is that, with the lowering of temperature, the incommensurate, collinear sinusoidal magnetic order locks into a non-collinear spiral magnetic order which gives rise to the spontaneous polarization. Nevertheless, the spiral magnets are not the only source of magnetism-induced ferroelectricity. The collinear E-phase magnetic structure has also been predicted to be the candidate wherein the magnetism-induced ferroelectricity polarization

can be about two orders of magnitude larger than that exhibited in the helical magnets [15, 16]. Indeed, large magnetoelectric effects and spontaneous electric polarization have been reported in the E-type orthorhombic $HoMnO_3$ and $YMnO_3$ [2, 3].

Furthermore, what role the rare earth plays in stabilizing the ferroelectricity is another interesting topic under discussion. In orthorhombic $HoMnO_3$, the considerable increase in polarization below 15K, where the Ho magnetic moment has a major change, suggests that the spontaneous polarization may involve rare earth moment [2]. A similar feature is shown in $DyMnO_3$, where the transformation of Dy magnetic moment form incommensurate structure to commensurate one causes ferroelectric polarization [17]. Besides, the lack of long-range magnetic order of Mn spins which is due to the paramagnetic fluctuation of Er^{3+} ion has been reported in orthorhombic $ErMnO_3$ [18]. Thus, the effects of rare earth elements could also be essential.

Understanding the complex mechanism of the coupling between magnetism and ferroelectricity remains a challenge, especially when the additional strain introduced to stabilize the desired crystal structure is involved. One way to refine our understanding of the effective magnetoelectric coupling in $RMnO_3$ systems is to explore how the structure, magnetic order, and rare earth affect ferroelectricity in orthorhombic $RMnO_3$ in a more systematic manner.

1.2. Motivation

In this study, we investigated the properties of orthorhombic $ErMnO_3$ (o-ErMO), which is a collinear E-type AFM material at low temperatures. Since it has been predicted that relatively strong ferroelectricity could arise in a collinear E-type magnetic structure [15] and an additional magnetic structure transition in o-ErMO has been confirmed and was also speculated as the ICM-AFM to E-type AFM transition through the heat capacity measurement [11], thus, o-ErMO is expected to exhibit enhanced behavior of magnetelectric coupling. In addition, as mentioned above, for $RMnO_3$ with the rare earth ionic size of R smaller than that of Dy thermodynamically stable structure is hexagonal structure. Therefore, for example, the o-ErMO samples studied previously were all prepared either by soft chemical procedures or by high-pressure synthesis and were all inevitable polycrystalline in nature. That had limited the capability to directly test the predicted properties along different orientations. As the difficulties in obtaining the single crystal o-ErMO are unavoidable, we prepared o-ErMO thin films to try to address the relevant issues. As shown in Fig. 1.1, since $ErMnO_3$ just locates beside $HoMnO_3$, which is on the verge of the transition point, it is more likely to obtain pure o-ErMO. Finally, o-ErMO provides a chance to study the role of the rare earth in affecting the magnetism and the associated ferroelectricity. In brief, the primary motivation of this study is to search for a potential prototype material exhibiting the intriguing magnetism-induced ferroelectricity by investigating the structure, magnetism, and rare earth properties of o-ErMO.

Chap.2

Fundamental physical properties of RMnO$_3$ manganites

In this study, we want to investigate the magnetism in o-ErMO, so we have to penetrate the fundamental basis for magnetic behavior in the manganites. The main source of magnetism in manganites is the result of the interaction among spins of magnetic Mn ions with partially filled d shells. The magnetic coupling between Mn d electrons via O p-orbital strongly depends on the d-orbital configurations. For example, superexchange and double exchange are primary interactions between spins of Mn ions and how they work is relevant to the d-orbital configurations. In the o-ErMO, Mn^{3+} ions linking atiferromagnetically are due to the superexchange, while the electron hopping from Mn^{2+} ions to Mn^{3+} producing ferromagnetic interaction is attributed to double exchange.
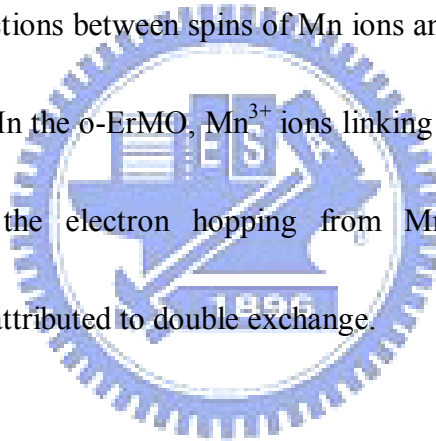
2.1 Superexchange

Superexchange is the magnetic coupling between two next-to-nearest neighboring magnetic positive ions through a non-magnetic anion. For example, the antiferromagnetic coupling occurs in Mn-O-Mn chain of MnO$_6$ octahedron crystal structure [19]. Fig 2.1 illustrates superexchange interaction by demonstrating schematically the spins in d orbitals of two Mn^{2+} ions separated by the p-orbital of a large O^{2-} ion (Fig. 2.1 (a)), and the corresponding changes when the sperexchange interaction prevails (Fig. 2.1 (b)).
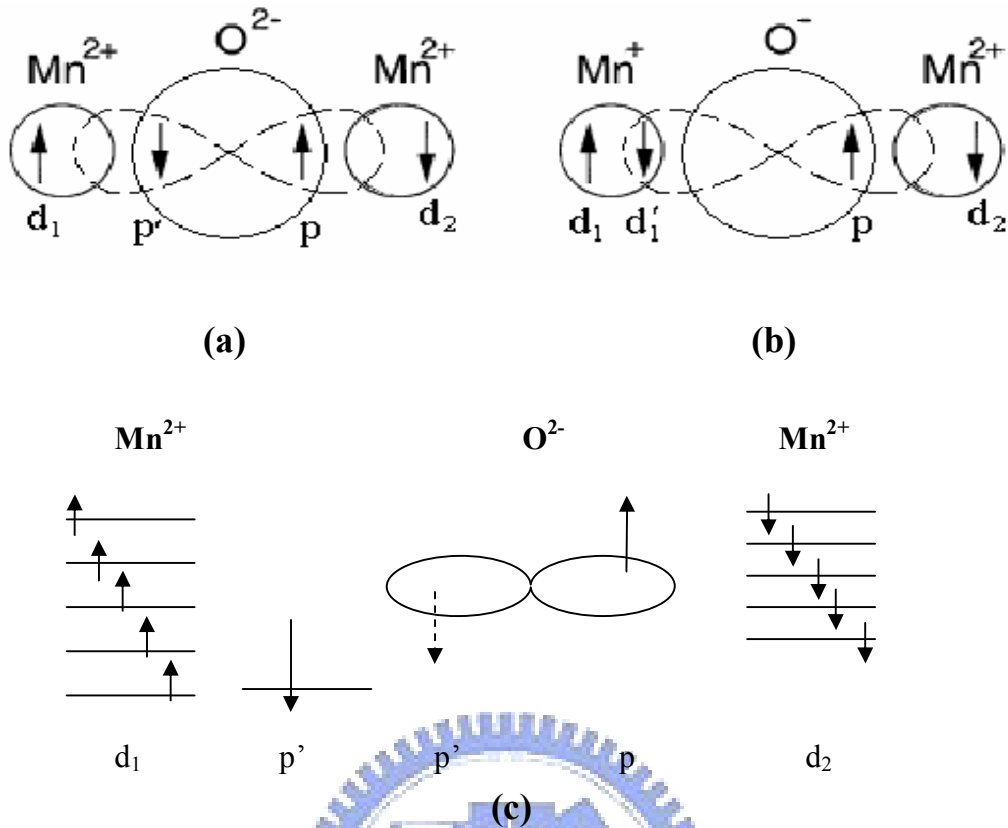
Fig. 2.1 The overlap between the wave functions of O^{2-} 2p and Mn^{2+} 3d orbitals for superexchange interaction. (a) Illustrating superexchange interaction by demonstrating schematically the spins in d orbitals of two Mn^{2+} ions separated by the p-orbital of a large O^{2-} ion (b) corresponding changes when the sperexchange interaction prevails (c) The mobility of electrons improves if the localized spins are polarized.

Since the distance between the Mn^{2+} ions is too large to result in direct interaction between them, the effect of kinetic exchange needs to be mediated via the covalent interaction between the Mn^{2+} ion and the O^{2-} ion orbitals. The hybridization of d and p orbitals nominally allows the p' electron to partially reoccupy the d_1 state of Mn^{2+} ions. According to Hund's rule, the spin of the electron in p' orbital of O^{2-} ion must be antiparallel to the spins of the electrons in d_1 orbital of Mn^{2+} ions. Besides, the remaining electron in p state has to be

antiparallel to the former one (electron in p') based on Pauli Exclusion Principle. Finally, the spins of the other Mn^{2+} ion (electrons in d_2) should be antiparallel to the spin of the remaining electron of O^{2-} ion (electron in p) due to the interaction between them. Therefore, the neighboring manganese ions are effectively coupled by the bridging of oxygen ion and form antiferromagnetic ordering.

2.2 Double Exchange

Double-exchange, originally proposed by Clarence Zener [20], is a mechanism that explains how electrons exchange between two species and why materials are ferromagnetic. For instance, the e_g orbitals of Mn ions could directly interact by the *2p* orbitals of O as a result of the electron hoppings among Mn^{3+}-O^{2-}-Mn^{4+} chain. The degeneracy of the *d* states of transition metal manganese is lifted and split into a double (e_g) and a triplet (t_{2g}) by crystal field. Hence, the configurations of Mn^{3+} and Mn^{4+} are denoted as $t_{2g}^3 e_g^1$ and $t_{2g}^3 e_g^0$, respectively. One electron in the *p*-orbital of O^{2-} ion hops onto the empty e_g orbital of Mn^{4+} ion and another electron in the e_g orbital of Mn^{3+} ion concurrently hops onto the *p*-orbital of O^{2-} ion.

This process is effectively equivalent to the effect that the electron directly hops form Mn^{3+} to Mn^{4+} and could be described as followings,

$$Mn_{1\uparrow}^{3+} O_{2\uparrow,3\downarrow} Mn^{4+} \rightarrow Mn^{4+} O_{1\uparrow,3\downarrow} Mn_{2\uparrow}^{3+}$$
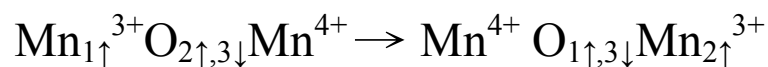
Furthermore, as governed by the Hund's rule and the Pauli exclusion principle, the magnetic

moments of these hopping electrons must be parallel to each other, leading to the

ferromagnetic alignment in two manganeses. However, the geometric shape of the

environment would affect the virtue of hopping. Namely, the effect is enhanced as the angle

between the orientations of the two spins is decreased [21]. The effectiveness is zero for

antiparallel spins, whereas the effectiveness is the largest for parallel ones.
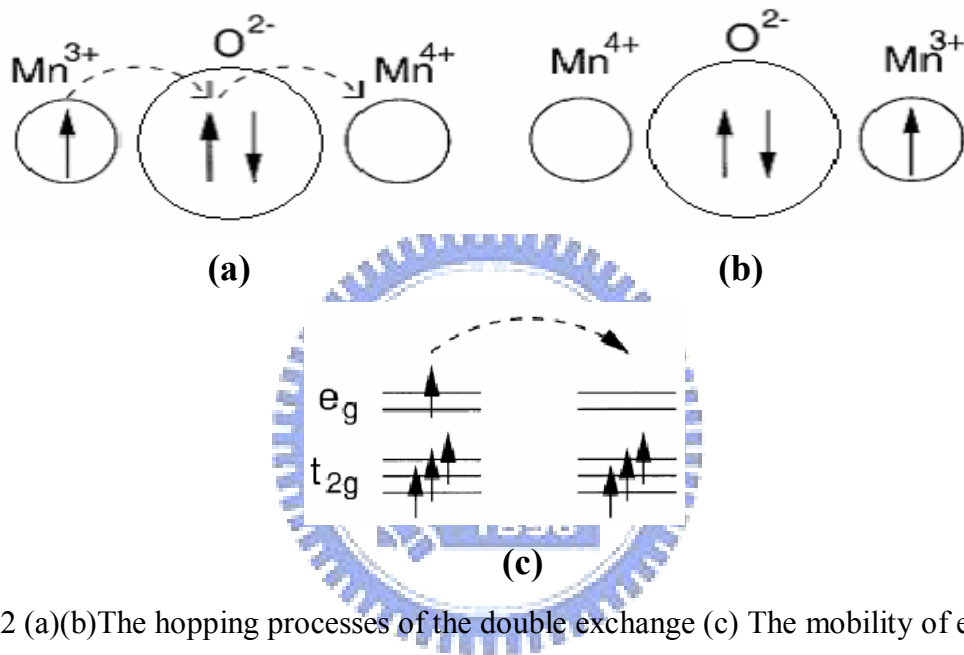
Fig. 2.2 (a)(b)The hopping processes of the double exchange (c) The mobility of electrons
improves if the localized spins are polarized.

2.3 The Crystal Field Effect

The presence of an electrical field between the neighboring ions will affect the energies

of the valence orbitals of the local ions. Since the localized electrons in d or f states are

influenced by the electrostatic field arising from the surrounding ions, the effect was called

crystal field. In this study, we only focus on the effect of octahedral crystal fields on

manganese oxide (MnO_6). Since lying along the Cartesian axes and pointing directly towards

the point charges, all *p* orbitals of Mn ions have the same degree of interaction with the ligands. Thus, *p* orbitals remain degenerate. However, the extra repulsion between the electrons in *p* orbitals and the point charges of the ligands raised the energies of *p* orbitals.
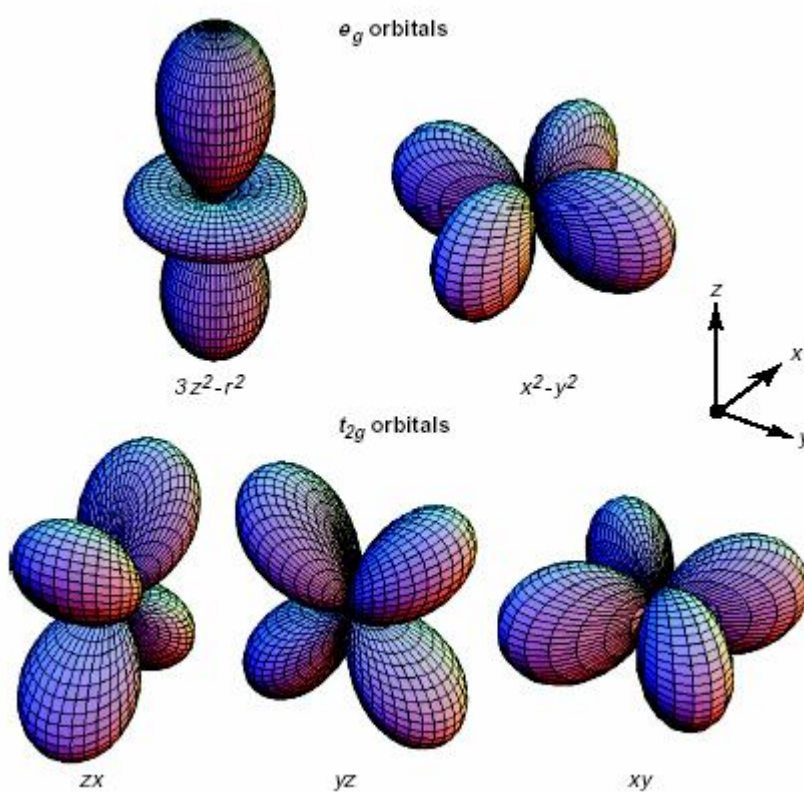
Fig. 2.3 The electronic distribution of five d orbitals [22]

On the other hand, repulsion between the electrons of the O^{2-} ions and the electrons in *3d* orbitals of the Mn ion in the MnO_6 octahedron not only increases but also splits the energy of these orbitals. In this octahedral field effect, the $3d_{x^2-y^2}$ and $3d_{3z^2-r^2}$ orbitals belong to the e_g symmetry group, while the $3d_{xy}$, $3d_{xz}$, and $3d_{yz}$ orbitals belong to the t_{2g} symmetry group. Two of *3d* orbitals ($3d_{x^2-y^2}$ and $3d_{3z^2-r^2}$) have lobes which point directly towards the point charges of the ligands, and so they have a greater electrostatic repulsion. The other three orbitals ($3d_{xy}$,

$3d_{xz}$, and $3d_{yz}$) have lobes which point toward the direction between the charges, and so have a weaker electrostatic repulsion. Furthermore, the energy difference between the two sets of orbitals from the $3d$ shell in the crystal field is 10Dq, where energy conservation suggests that the energies of the t_{2g} orbitals be lowered by 4Dq and the e_g orbitals be raised by 6Dq [23]. Where 10Dq is ligand field splitting parameter.
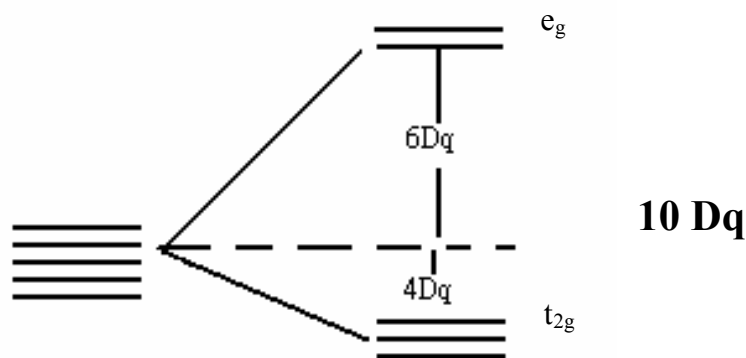
Fig. 2.4 Split energies of 3d orbitals in octahedral crystal field

2.4 The Jahn-Teller Effect

For highly symmetrical molecules, there always exists at least one non-totally symmetric vibration that makes electronically degenerate states unstable. This instability would distort the crystal, reduce its symmetry and lower its energy to break the degeneracy. The appearance of this distortion is the Jahn-Teller effect [24]. Assuming that the octahedron is elongated along the z-axis, then, since the repulsion between the electron in $3d_{3z^2-r^2}$ orbital and the ligand decreases, the energy of $3d_{3z^2-r^2}$ orbital is lower. On the contrary, as an electron in $3d_{x^2-y^2}$ orbital is repelled by the shortened ligands on the x- and y-axis, the energy of $3d_{x^2-y^2}$ orbital is raised. Thus, the degeneracy of e_g orbitals would be lifted. The $3d_{xy}$, similar to $d_{x^2-y^2}$,

is repelled by the closer ligands on the *x*- and *y*-axis, whereas $3d_{yz}$ and $3d_{xz}$, similar to $3d_{3z^2-r^2}$, are lowered in energy since the electrons occupying these states experience weaker repulsion from the longer ligands on the *z*-axis. Hence, the t_{2g} state would also split into two states. Similarly, the compression on the *z*-axis will lower the energy level of the $3d_{x^2-y^2}$ and $3d_{xy}$ orbitals and raise the energy of the $3d_{3z^2-r^2}$, $3d_{yz}$ and $3d_{xz}$ levels. The processes are depicted schematically in Fig. 2.5 shown below.
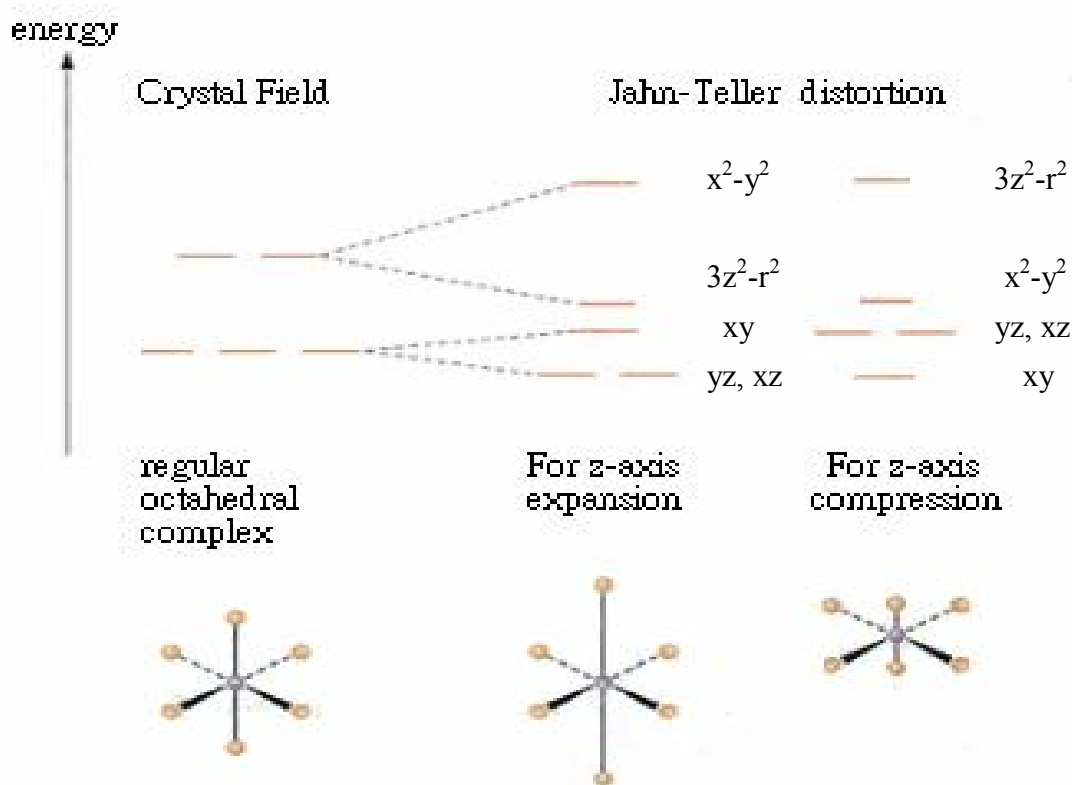
Fig. 2.5 Energy splittings of the Mn 3*d* orbitals due to Jahn-Teller effect [25]

It is also worth noting that the Jahn-Teller distortions are relatively strong in complexes with d^4 (high spin) and d^9 configuration in comparison with d^1, d^2, d^4 (low spin), d^5 (low spin), d^6 (high spin) and d^7 (high spin), where the degeneracy is t_{2g} state. The orbitals of t_{2g} state do

not direct toward ligands so the splittings is smaller.

2.5 Crystal structure of the orthorhombic manganites (RMnO$_3$)

Orthorhombic RMnO$_3$ belongs to perovskite-structure oxides, ABO$_3$, which have the prototypical cubic structure shown in Figure 2.6. The cubic perovskite structure is characterized by a cation, B, residing at the center of the octahedron, which is surrounded by six oxygen anions, with another cation, A, locating at the corner of the unit cell. Where A and B are R and Mn, respectively [26]. As shown in Fig. 2.6, six oxygen anions bond with Mn to form an octahedron. The degenerate energy states of $3d$ orbitals would split into two energy levels (e$_g$ and t$_{2g}$) due to the influence of crystal field. The degeneracy of these two levels would be lifted again due to the Jahn-teller distortion. The lattice constants, bond length between Mn and O and bond angle of Mn-O-Mn would be adjusted as a consequence of the Jahn-Teller effect experienced by different rare earth elements. There is a tendency that the smaller ions size is, the stronger the Jahn-Teller effect is [27].
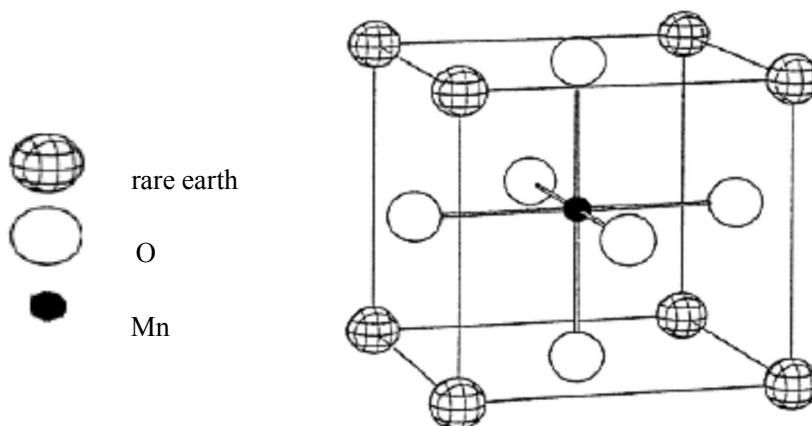
Fig. 2.6 The perovskite structure

Moreover, the serial compounds of orthorhombic $RMnO_3$ are usually described by *Pbnm* and *Pnma* space groups. In addition to primitive, there are three parts of the space group symbol indicating the symmetry with respect to the *x*, *y*, and *z* axis directions, respectively. Thus, for example, the space group symbol *Pnma* indicates a primitive lattice with an n-glide plane perpendicular to the x axis, a mirror plane perpendicular to the y axis, and an a-glide plane perpendicular to the z axis. In this work, we use *Pbnm* type to depict the crystal symmetry, but these two types could be converted to each other.

2.6 Models for magnetic structure of orthorhombic $RMnO_3$
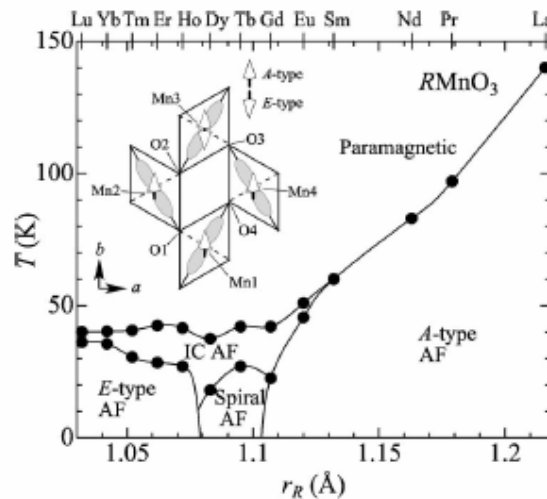
Fig. 2.7 The phase diagram of orthorhombic $RMnO_3$ [11]

The magnetic structure evolves with the ion size of rare earth elements according to the phase diagram reported by Makoto Tachibana *et al.* [11] For R=La-Sm, A-type antiferromagnetic (AF) order is induced by in-plane orbital order below the Neel temperature, T_N, which decreases gradually with reducing ion size. For R=Eu and Gd, a sinusoidal incommensurate (IC) structure, where a vector (0, q, 0) describing the periodicity of the

A-type structure will modulate with temperature on cooling. This IC structure also subsists

with increasing q ($0 < q \leq 0.5$) for smaller ions. However, the A-type AF structure does not

remain steady as the ion size is smaller than that of Gd. The IC structure transforms to a spiral

structure as temperature decreasing for R= Tb and Dy, while it locks to the E-type AF

structure with q= 0.5 for R=Ho-Lu. Several common magnetic structures relevant to the

orthorhombic $RMnO_3$ are listed as follows:

The A-type magnetic structure

In this case, the spins exhibit ferromagnetic (FM) order within the *ab* plane and

antiparallel antiferromagnetic (AF) interplanar couplings.
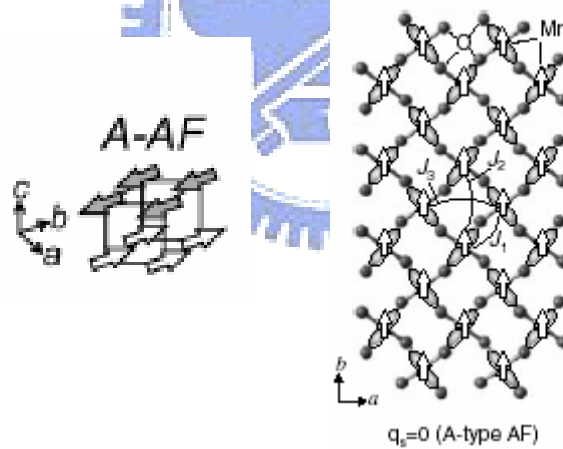
Fig. 2.8 A-type magnetic structure [17,26] the arrows indicate the spins of Mn^{3+}

The spiral magnetic structure

An incommensurate spiral structure has spins rotate in one plane, which breaks spatial

inversion symmetry to induce polarization. For example, the spins rotate in the *bc* plane in

$TbMnO_3$ as temperaure is below T_{lock}.

(a)
(b)
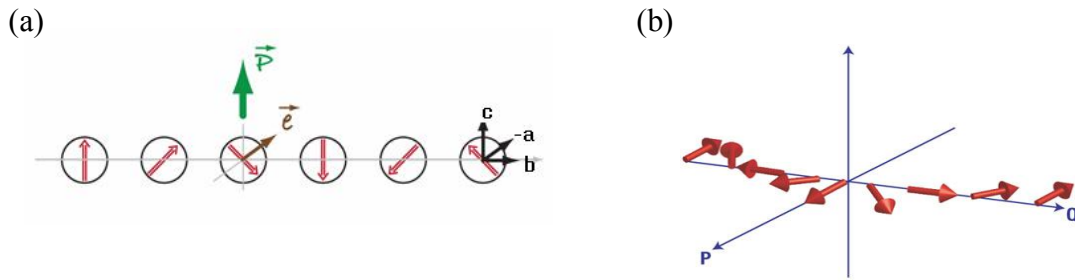
Fig. 2.9 (a) The spiral magnetic structure with spins rotating in the (*b*, *c*)-plane [28] (b)
polarization(**P**) lies in the plane of the spiral, but perpendicular to its propagation vector
Q [29]

The E-type magnetic structure

The E-type AF structure, where the existence of large polarization is predicted, is
characterized by FM and AF arrangement along the *a* and *b* axes with q = 0.5, respectively.
The interplanar coupling is also AF coupling in this case.
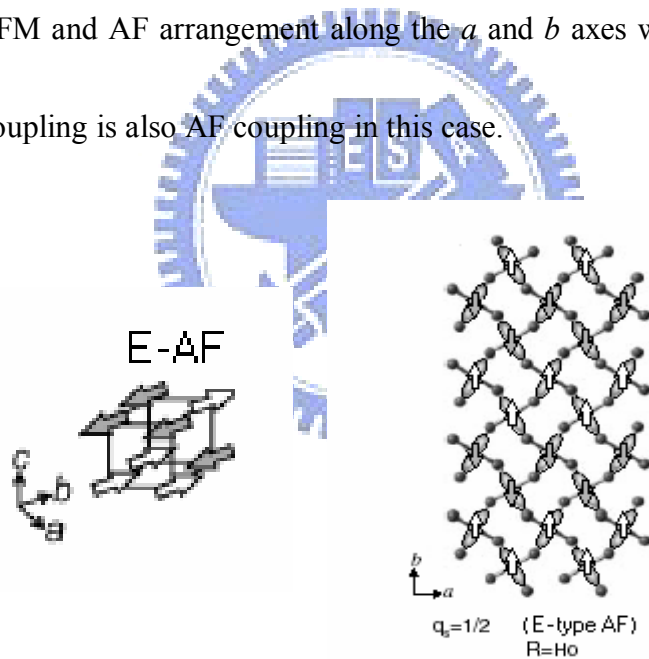
Fig. 2.10 The E-type magnetic structure [17, 26] the arrows indicate the spins of Mn^{3+}

The sinusoidal magnetic ordering

The sinusoidal spin order, similar to the E-type one, has a wave vector propagating
along the *b* axis and has zigzag chains of parallel spins on the *ab* plane directing along the *a*
axis. However, unlike the E-type AF, the magnitude of sinusoidal spins modulates in

neighboring zigzag chains with incommensurate wave q ($0 < q < 0.5$).

$q_s = 0.28$ (sinusoidal)
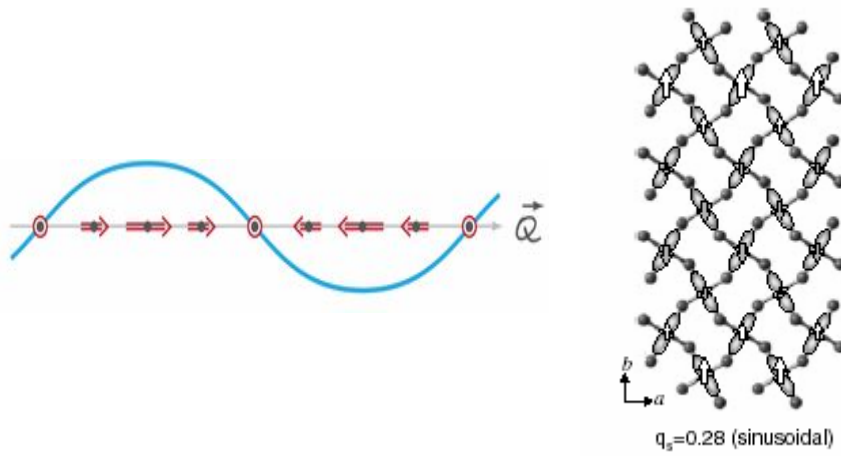
Fig. 2.11 (a) The sinusoidal spin density wave, in which spins point along one direction but

vary in magnitude (b) The sinusoidal spin structure [26, 28]
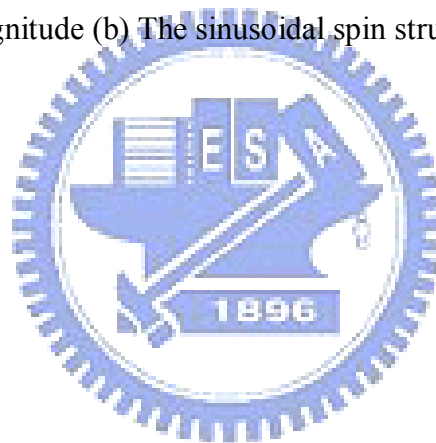
Chap.3 Experiments

3.1 Sample Preparation

3.1.1 Target Fabrication

The hexagonal $ErMnO_3$ bulk prepared by solid-state reaction methods were used as target for pulsed laser deposition. We start with mixing the $MnCO_3$ (99.95%) and Er_2O_3 (99.9%) powders with proper proportions and preheat the mixture at 1100℃ for 8 hours to fully facilitate reactions among the constituents. The solidified mixture was then pressed, ground and sintered at 1350℃ for 36 hours. After repeating the above process three times, we pressed the product into pellet for final sintering process conducted at 1350℃ for 36 hours. To promote the crystalline quality of the sintered pellet, the increment of heating and cooling was kept at 5℃ per minute during the process.

3.1.2 Pulsed Laser Deposition (PLD)

PLD [30] is essentially a physical vapor deposition process viable for fabricating thin films with complicated stoichiometry. In PLD process, a high energy laser pulse is focused on the surface of a solid target to explosively evaporate the target material. After absorbing strong electromagnetic radiation, local area of the solid target is instantaneously vaporized to form a laser plume which would be deposited on chosen substrate. When grown on proper substrates and under appropriate conditions, the structure of $ErMnO_3$ transforms from hexagonal to orthorhombic during deposition by the effect of strain. To optimize the

deposition conditions, the films were grown by 248nm KrF excimer laser with laser energy

density modulating from 2 to 4 J/cm^2, repetition rate varying from 3 Hz to10 Hz, substrate

temperature (T_s) changing from 700℃ to 880℃, and oxygen pressure ranging between 0.1

torr to 10^{-4} torr.
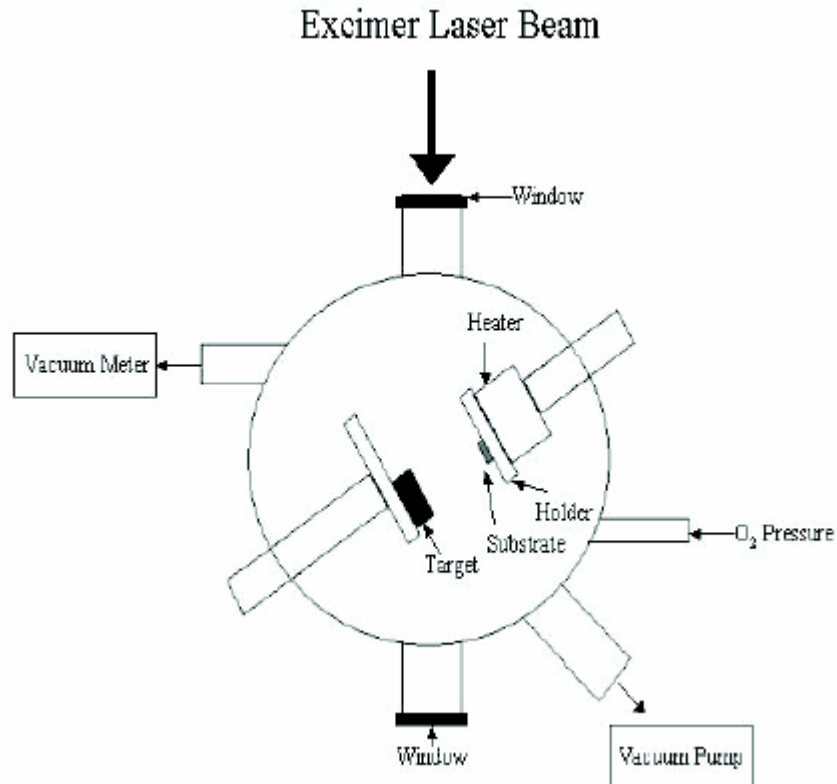
Fig.3.1 The configuration of PLD system

A schematic diagram of the PLD system is shown in Fig. 3.1, and the detailed

procedures for preparing the o-ErMO films are described below：

1. Clean the substrate in acetone, methanol, and DI water under ultrasonic vibration for 5

minutes, respectively.

2. Repeat above processes for 3 times.

3. Attach the substrate on the stainless steel plate by silver paste.

4. Heat the plate at 150 ℃ till the silver paste is solidified.

5. Clean the surface of substrate by nitrogen gas.

6. Put the plate in the chamber of PLD system with thermal couple imbedded.

7. Pump the chamber till the base pressure is lower than 10^{-6}torr for 1 hour at least.

8. Heat the substrate to the preset temperature.

9. Aerate the chamber with oxygen to the expected pressure.

10. Set the power, repetition rate and counts of excimer pulsed laser.

11. Start to deposit the film on the substrate.

12. Cool the thin film in 400 torr O_2 environment to room temperature with the heater off.

13. Take out the sample.
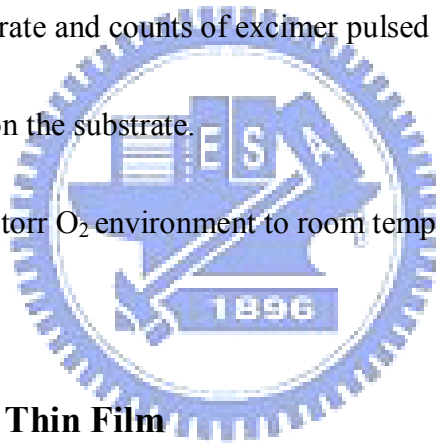
3.2 Characterization of Thin Film

3.2.1 X-ray diffraction (XRD)

We analyzed the crystal structure of $ErMnO_3$ by X-ray diffraction (XRD) measurements. XRD [31] is a rapid analytical technique to measure the average spacing between layers or rows of atoms, determine the orientation of crystal and find the crystal structure of an unknown material. The diffraction pattern of XRD is described by Bragg's law.

$$2d \sin \theta = n \lambda$$
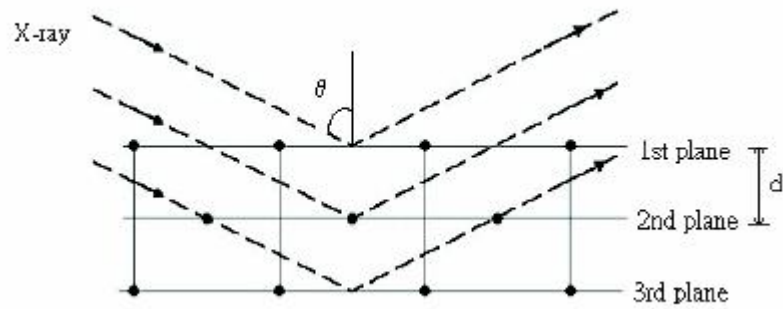
Fig. 3.2 The schematic illustration of the XRD process

Where d is the distance between successive parallel planes, θ is the angle between the incident

X-ray and the normal of the lattice plane, n is an integer, and λ is the wavelength of the X-ray.

XRD can also be used as a tool for the preliminary analysis of composition. The simple

schematic illustration of XRD is shown in Fig. 3.2.

3.2.2 α-step profilometer
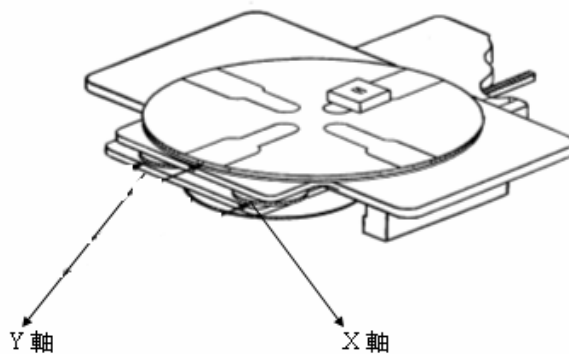
Fig. 3.3 The configuration of α step profilometer

Alpha-step profilometer is an instrument probing the surface profile of a surface and is

used to measure the thickness of thin film. This instrument consists of a stylus that is dragged

across the surface while maintaining a constant vertical contact force. The stylus thus follows

21

the topography of the sample, and the height profile is recorded. According to the height profile, the thickness and roughness are assessed.

3.2.3 X-ray reflectivity (XRR)

X-ray reflectivity (XRR) is a technique for precise measurement of the thickness of a thin layer. When impinged on a sample below the critical incidence angle, which is related to the material of the film, XRR exhibits total external reflection. In contrast, as the angle of reflection is increased to exceed the critical angle, X-ray penetration occurs and the X-ray reflected from the buried interface interfere with surface reflected radiation to give rise to interference fringes. Therefore, the thickness and interfacial roughness of the sample could be measured. Because this technique does not rely upon material crystalline, it can be used to characterize amorphous as well as crystalline layers. In this study, we obtain the thickness of thin film by the periodicity of the obtained Kiessig fringe. $T \approx \dfrac{2\pi}{\Delta q}$ Where T is the thickness and Δq is periodicity of Kiessig fringe.

3.2.4 Four-circle diffractometer (Φscan)

Four-circle diffractometer, where the four circles are θ, χ, Φ, and 2θ, was used to determine the texture, lattice parameters, and epitaxial relationship between film and substrate. It is an instrument frequently used in X-ray crystallography to determine the shape and symmetry of the unit cell of the film. After placed in the goniometer head with an arbitrary orientation, the film is illuminated and rotated to measure the intensity of the diffracted

radiation as a function of beam and sample orientation. If the dimensions of the unit cell were known, they can be used to calculate the settings of the four angles needed to observe a specific orientation.
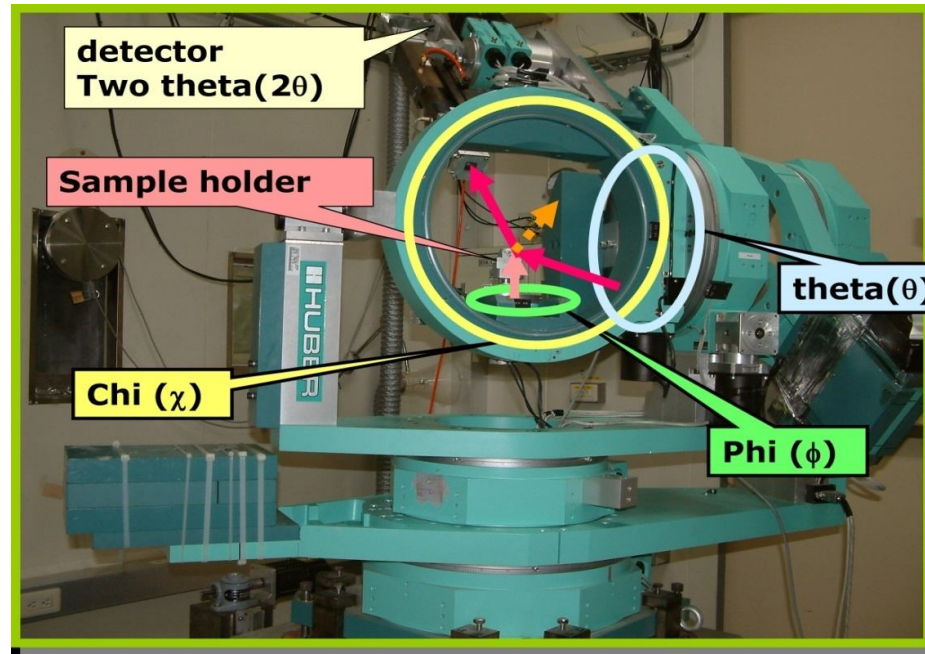
Fig. 3.4 Four-circle diffractometer

3.2.5 Superconducting Quantum Interference Device (SQUID)

SQUID [32] is a delicate equipment integrating electronic, mechanical, low-temperature, and vacuum techniques for measuring magnetization with extremely high sensitivity and precision. SQUID combines two Josephson junctions connecting in parallel. It is used to measure extremely weak signals and its sensitivity is about 10^{-8} emu with 0.1T external magnetic field applied. The Josephson junction often consists of a tunnel barrier sandwiched between two superconducting electrodes. A much more sensitive direct current (DC) SQUID consists of two parallel Josephson junctions in a loop of inductance L so that

electrons tunneling through the junctions demonstrate quantum interference, dependent on the strength of the external magnetic field within a loop. Since demonstrating resistance in response to even slight variations in a magnetic field, DC SQUID is presently the most sensitive magnetometer available.

Fig. 3.5 Superconducting Quantum Interference Device

3.2.6 X-ray Absorption Near Edge Spectroscopy (XANES)

X-ray absorption spectroscopy (XAS) is an essential tool to detect electronic structures of specific atoms in a solid. When the x-rays hit a sample, the oscillating electric field of the electromagnetic radiation interacts with the electrons bound in an atom. The radiation will be either scattered or absorbed by these electrons and then the electrons are excited.
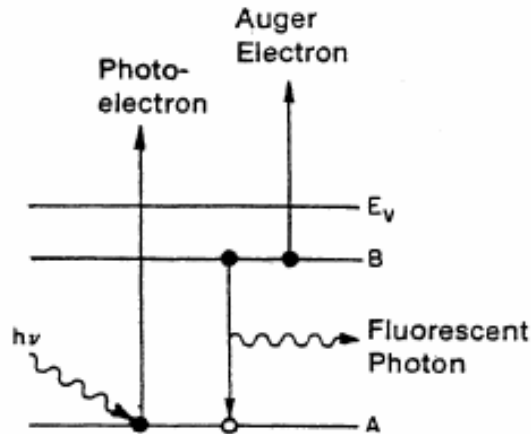
Fig. 3.6 The schematic demonstration of the typical processes involved in XAS

When the energy of the incident photons is just sufficient to cause excitations of the core electrons in the absorbing atom to a continuum state by dipole selection rule with no spin changes, absorption edge will occur. The resulting core hole is filled by the capture of an electron from another shell followed by the emission of a fluorescent photon, most of which further excites the Auger electron. Then, the spectrum of fluorescence photon and Auger electrons can delineate the change in relevant electronic structure. The energies of the absorbed radiation at these edges correspond to the binding energies of electrons in the K, L, M, etc., shells of the absorbing elements. The absorption edges are labeled in the order of increasing energy K, L_I, L_{II}, L_{III}, M_I, corresponding to the excitation of an electron from the 1s $(2S_{\frac{1}{2}})$, 2s $(2S_{\frac{1}{2}})$, 2p $(2P_{\frac{1}{2}})$, 2p $(2P_{3/2})$, 3s $(2S_{\frac{1}{2}})$ orbital (state), respectively.
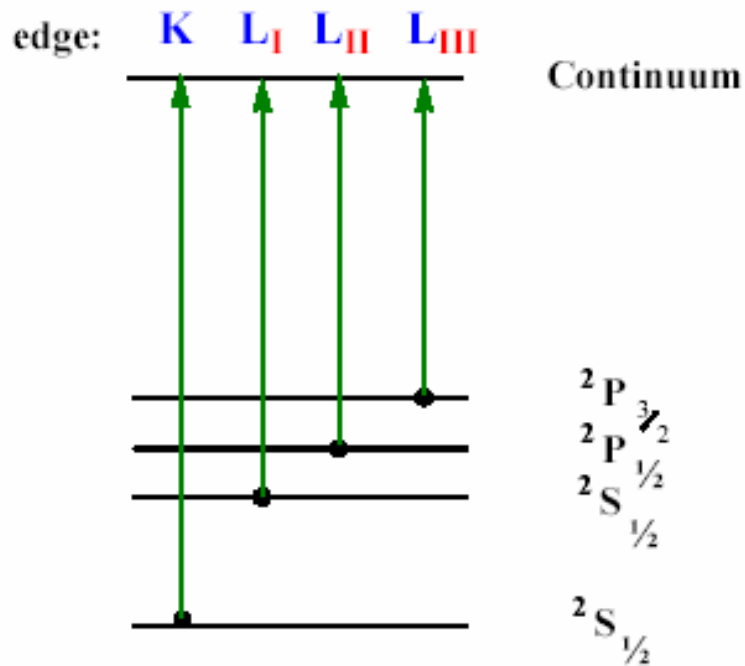
Fig.3.7 The label of the absorption edges

An x-ray absorption spectrum is generally divided into four regimes: 1) pre-edge (E <

E_0); 2) x-ray absorption near edge structure (XANES), where the energy of the incident x-ray

beam is $E = E_0 \pm 10$ eV; 3) near edge x-ray absorption fine structure (NEXAFS), in the region

between 10 eV up to 50 eV above the edge; and 4) extended x-ray absorption fine structure

(EXAFS), which starts approximately from 50 eV and continues up to 1000 eV above the

edge. Where E is the energy of photoelectrons and E_0 is the binding energy. We only focus

XANES in this study.

Chap.4 Results and Discussion

4.1 The structural and magnetic properties of target

The hexagonal ErMO₃ (h-ErMO) bulk prepared by solid-state reaction method was used as target for PLD to deposit o-ErMO thin films. In order to make high quality thin film, it is essential to fabricate good quality target. Before pressing the ErMnO₃ to produce sample pellet, we tuned the heating temperature from 1100℃ to 1400℃ to optimize the sintering condition. As shown in Fig. 4.1, the XRD pattern of h-ErMnO3 powder sintered at different temperatures indicated that 1350℃ was the most suitable temperature for target due to the extent of independence of the peaks and the fineness of them.
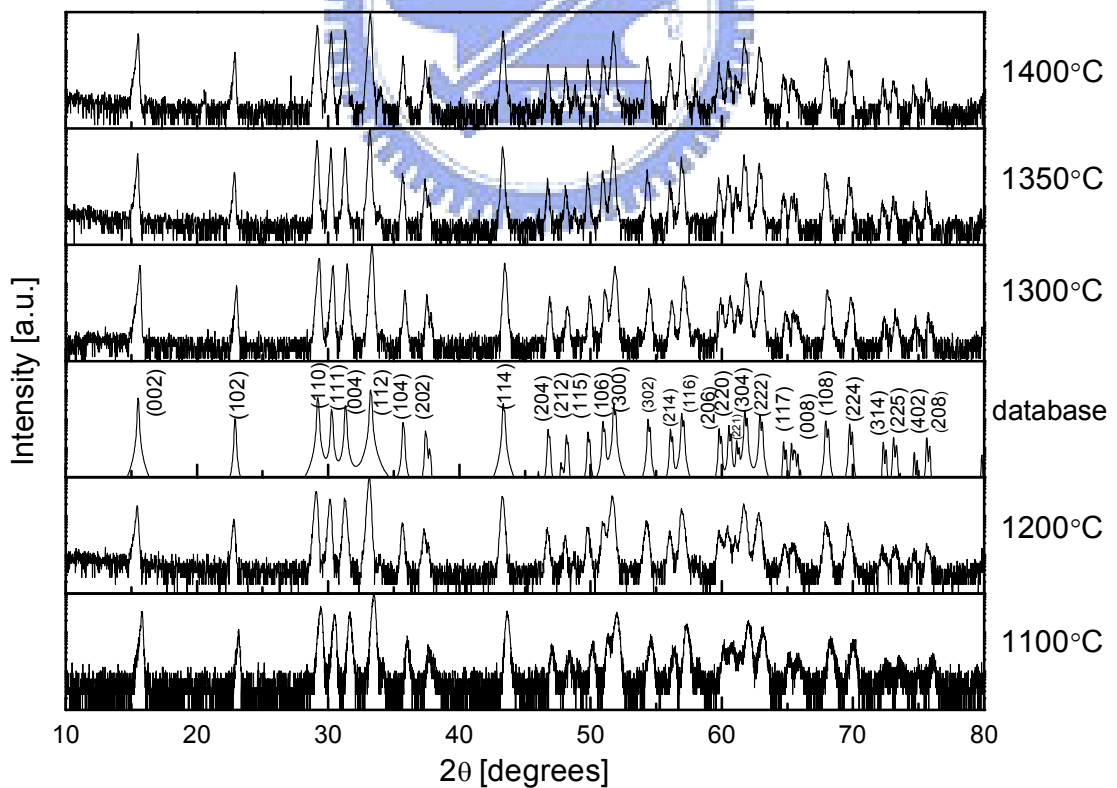
Fig. 4.1 The XRD θ-2θ patterns of h-ErMO powder as a function of sintering temperature

14-0689   Quality: *

CAS Number:

Molecular Weight: 270.20
Volume[CD]: 370.50
Dx: 7.266   Dm:

S.G.: P6₃cm (185)
Cell Parameters:
a 6.116 b   c 11.43
α   β   γ

SS/FOM: F30=67(.0093, 48)
I/Icor:
Rad: CuKa1
Lambda: 1.5405
Filter: Ni
d-sp:

Er Mn O3
Erbium Manganese Oxide
Ref: Natl. Bur. Stand. (U.S.) Monogr. 25, 2, 16 (1963)

2θ	Int-f	h k l	2θ	Int-f	h k l	2θ	Int-f	h k l
15.486	30	0 0 2	51.721	45	3 0 0	74.577	2	2 2 5
22.871	10	1 0 2	54.319	10	3 0 2	75.538	2	2 0 8
29.168	50	1 1 0	56.040	6	2 1 4	80.460	6	2 2 6
30.218	35	1 1 1	56.894	20	1 1 6	82.898	6	3 1 6
31.270	35	0 0 4	59.722	6	2 0 6	83.583	4	4 1 0
33.214	100	1 1 2	60.498	8	2 2 0	84.047	2	4 1 1
35.654	8	1 0 4	61.090	4	2 2 1	85.661	10	4 1 2
37.391	6	2 0 2	61.690	25	3 0 4	87.056	6	3 2 4
37.684	4	1 1 3	62.870	16	2 2 2	87.114	4	1 0 10
43.295	40	1 1 4	64.628	4	1 1 7	87.793	4	3 0 8
46.684	6	2 0 4	65.192	2	0 0 8	90.179	<1	4 0 6
48.101	4	2 1 2	67.851	10	1 0 8	91.920	8	4 1 4
49.748	6	1 1 5	69.690	8	2 2 4			
50.880	10	1 0 6	72.238	2	3 1 4			

Fig. 4.2 The XRD θ-2θ patterns of h-ErMO from database

Temperature dependent magnetization *M(T)*, inverse susceptibility χ^{-1}(T) and difference in *M(T)* between field-cooled (FC) and zero-field-cooled (ZFC) of h-ErMnO3 powder scraped from the target are shown in Fig. 4.3. In addition to structural properties, the Neel temperature, observed at 74K in magnetization *M(T)*, also exhibits the characteristic of h-ErMO, which is consistent with previous results [33,34].
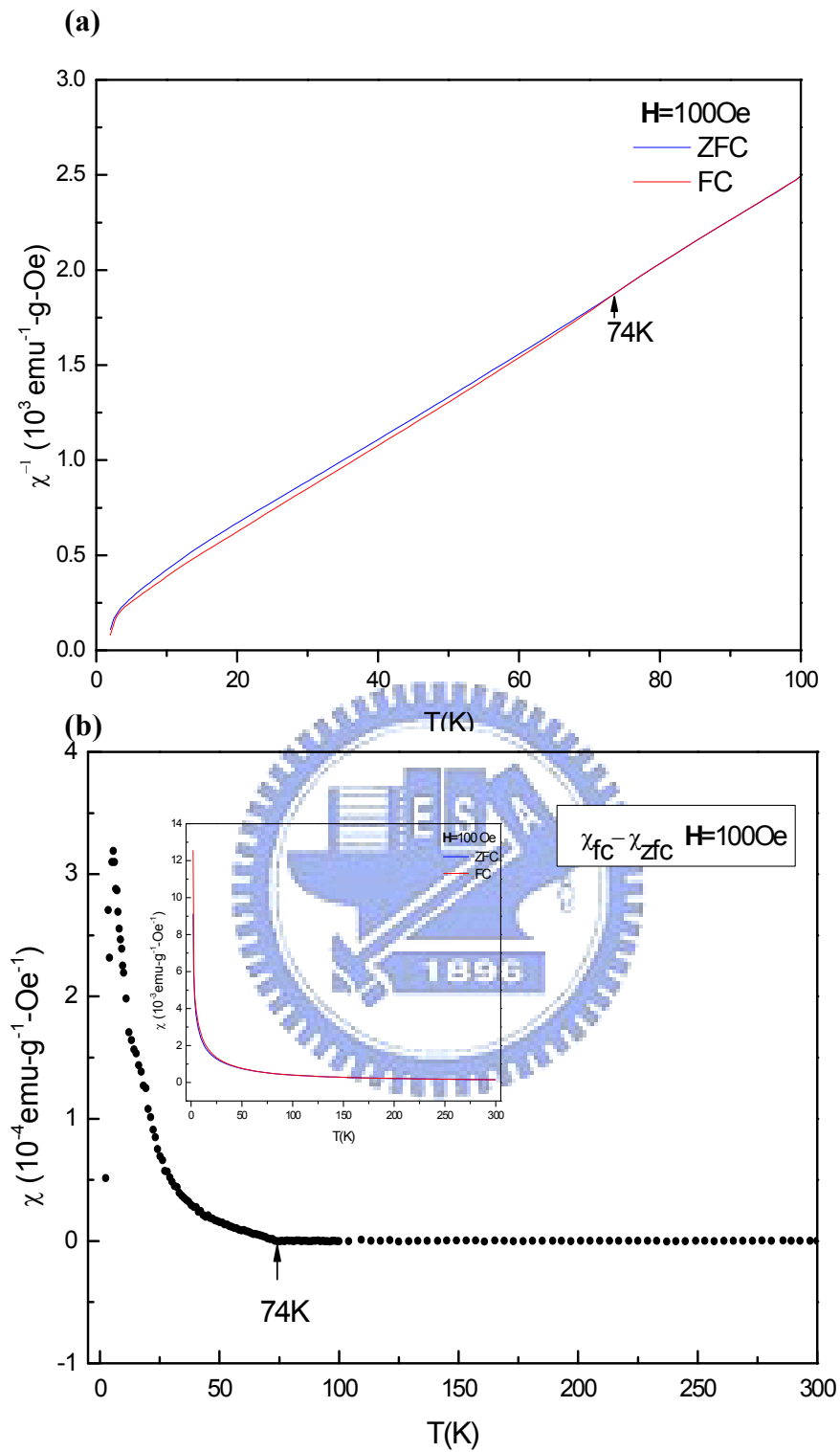
Fig. 4.3 (a) Temperature dependence of the inverse susceptibility $\chi^{-1}(T)$; (b) difference in *M(T)*

between field-cooled (FC) and zero-field-cooled (ZFC) of h-ErMO powder Inset of (b) shows

the temperature dependent magnetization *M(T)*

4.2 The characterization of o-ErMO thin film

4.2.1 The structural properties

When grown on proper substrates and under appropriate conditions, the orthorhombic structure of $ErMnO_3$ can be stabilized by the epitaxial strain between film and substrate during PLD process. To optimize the deposition conditions, the films were grown by using KrF excimer laser with laser energy density modulating from 2 to 4 Jcm^{-2}, repetition rate varying from 3 Hz to10 Hz, substrate temperature changing from 700℃ to 880℃, and oxygen pressure ranging between 0.1 torr to 6×10^{-4} torr. Fig. 4.4 show the XRD θ-2θ patterns of o-ErMO films deposited on $LaAlO_3$ (110) [LAO (110)] substrate at different substrate temperatures (T_s) and various oxygen pressures (P_{O_2}). The (020) peak diffraction peak of o-ErMO appears to shift toward lower 2θ angles with increasing T_s, indicating that the b lattice constant is increasing, presumably due to the relation of compressive strain along b-axis. Similar trend was also observed with decreasing oxygen partial pressure during deposition. One of the possible reasons for this is that at low P_{O_2} environment, since colliding with fewer particles, the evaporated particles arriving the substrate surface are left with higher kinetic energy and higher mobility on the substrate. A kin to those deposited at higher substrate temperatures, the higher surface mobility of the arriving particles might accommodate to the substrate better and lead to less in-plane tensile strain between substrate and the growing film. As a result, the compressive strain along the b-axis due to the in-plane

stretching in *a* and *c* direction will be somewhat eased and result in increasing lattice constant

of the *b*-axis.
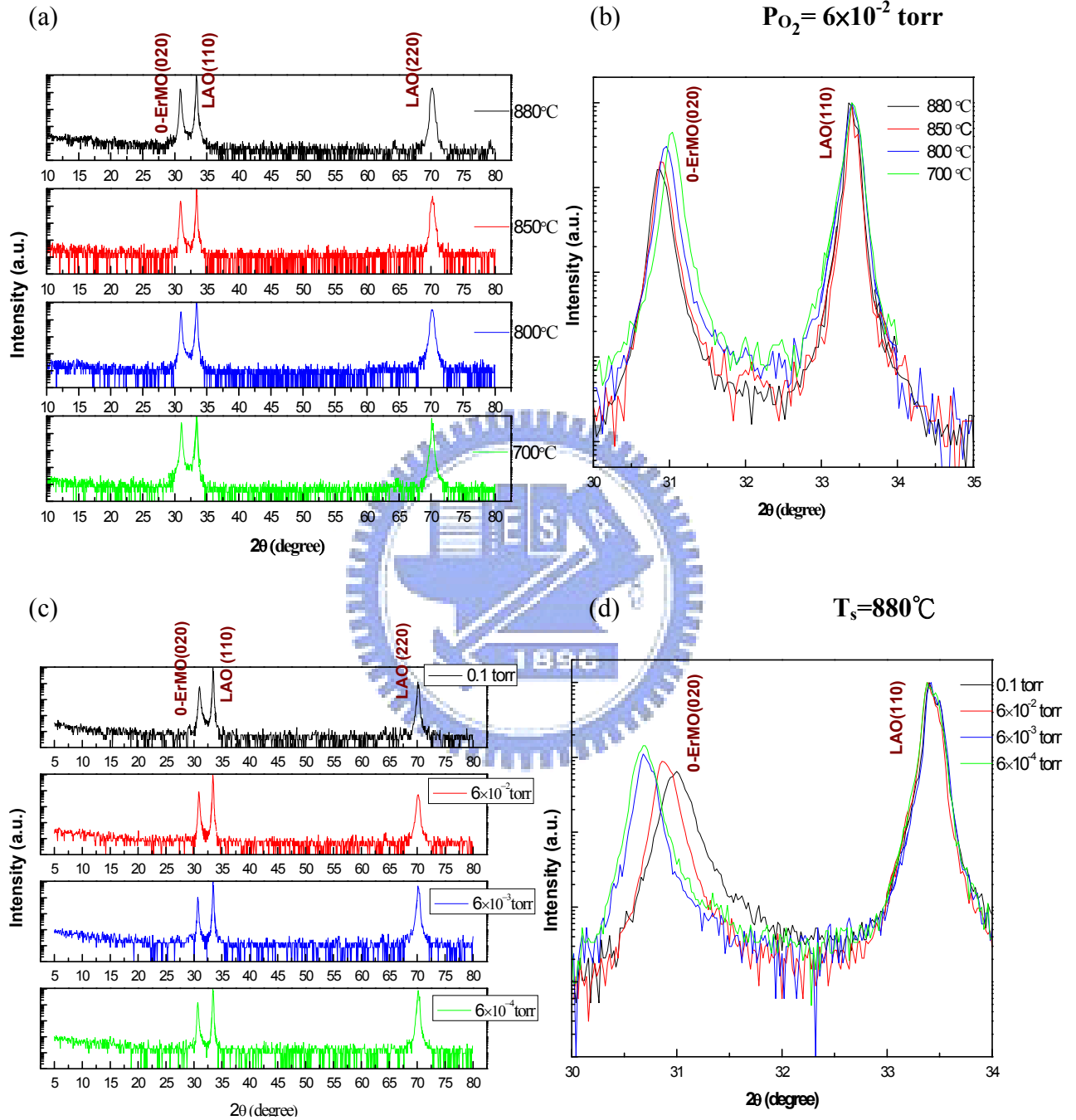
Fig. 4.4 XRD pattern of o-ErMO/LAO(110)

(a)(b) At different substrate temperatures (c)(d) At different oxygen pressures

The full width at half maximum intensity (FWHM) of the rocking curves taken at

o-ErMO(020) diffraction peak of all samples grown at different pressures and different

temperatures are listed in Table 4.1. These data were obtained by fitting the measured (020)

peaks of o-ErMO with Gaussian function. The progressive improvements of the FWHM with

either increasing substrate temperatur or decreasing oxygen pressure indicate that the

crystalline quality of the film is improved with the same trend. The smallest FWHM was $0.47°$

for the film grown at $880℃$ and $6×10^{-4}$ torr; thus, this condition was chosen as optimal

condition in the beginning.

Table 4.1 The FWHM for the films grown at various substrate temperature and different
oxygen pressure

$P_{O_2}= 6×10^{-2}$ torr   **$T_s=880℃$**

Temperature (℃)	FWHM(°)	Pressure (to rr)	FWHM(°)
700	0.996	$1×10^{-1}$	0.774
800	0.817	$6×10^{-2}$	0.691
850	0.726	$6×10^{-3}$	0.489
880	0.687	$6×10^{-4}$	0.466

However, φ-scans of the o-ErMO(110) peak for $P_{O_2}=6×10^{-4}$ torr indicated three pairs of

twofold symmetry, where one was well aligned with the twofold symmetry of LAO(100) and

the others shifted 70 degrees with respect to the preceding twofold symmetry (Fig. 4.6). This

result revealed that the film for $P_{O_2}=6×10^{-4}$ torr exhibits a twin-like structure with diagonal

line coincidence. By comparing with previous results [6, 7], depositing films in low P_{O_2} circumstance was the main reason to cause this twin-like structure. In order to compromise the film quality against epitaxial relations between film and substrate, the optimal condition was modified to $T_s= 880℃$ and $P_{O_2}=6\times10^{-2}$ torr. At these modified conditions, φ-scans of the film (Fig. 4.7) showed that the film deposited at $P_{O_2} = 6\times10^{-2}$ torr was a perfectly twofold symmetry indicating the film is having an excellent orthorhombic structure with three crystal orientations distinctively aligned with the substrate. Fig. 4.8 shows the spindle-like grains of o-ErMO in the AFM image, suggesting that the film align in the specific crystallographic directions of LAO (LAO[001]//o-ErMO(001) and LAO[1-10]//o-ErMO[100]). Thus, it was clear that a-axis could be differentiated from c-axis by anisotropic shape of the grain morphologies.
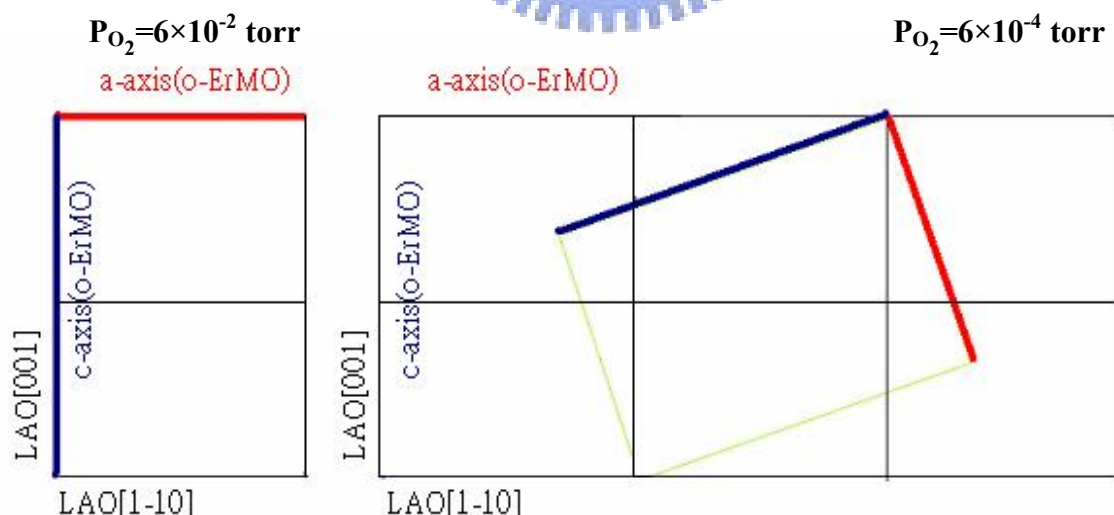
Fig. 4.5 In-plan arrangements between the o-ErMO thin films and LAO(110) substrate
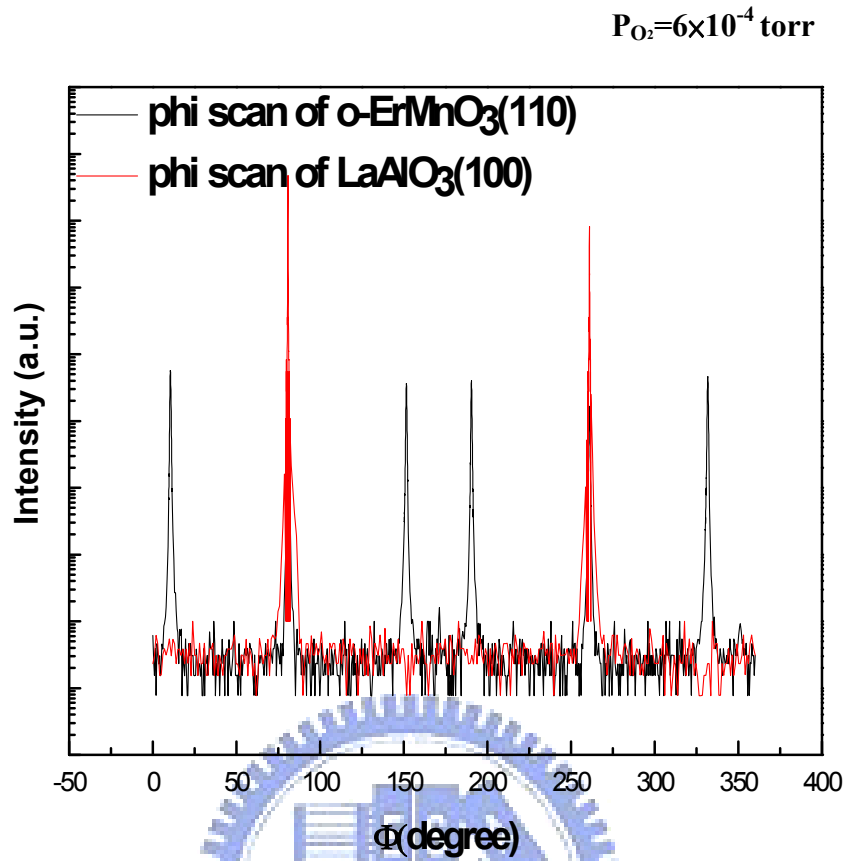
$P_{O_2}=6\times10^{-4}$ torr

Fig. 4.6 The φ-scans of the o-ErMO/LAO (110) thin film deposited at $P_{O_2}=6\times10^{-4}$ torr
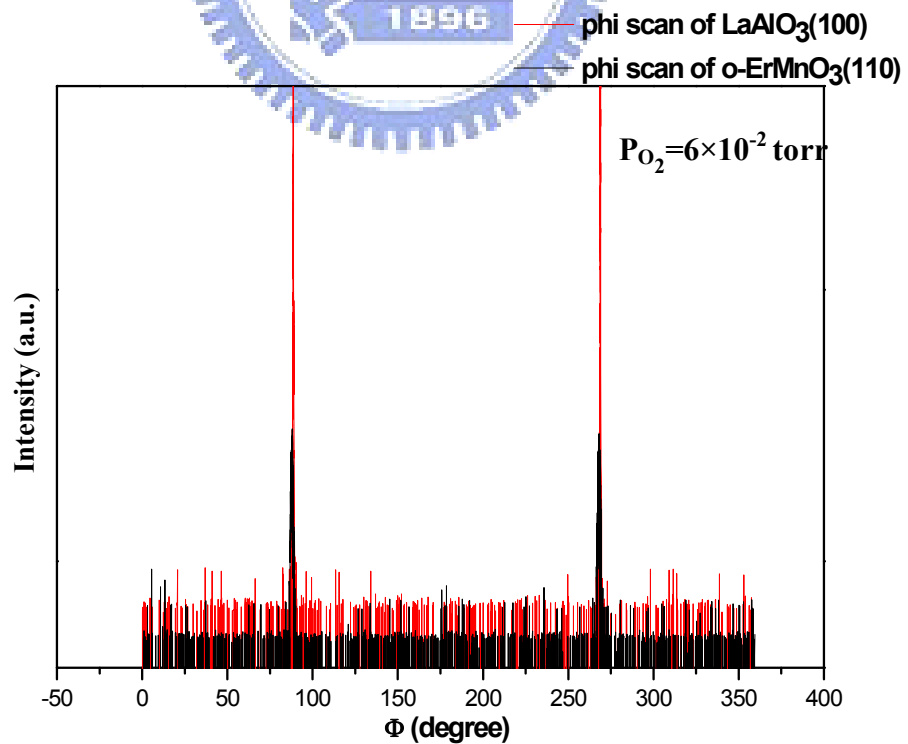
Fig. 4.7 The φ-scans of the o-ErMO/LAO thin film deposited at $P_{O_2}=6\times10^{-2}$ torr

$R_a=0.521$ nm

$R_q=0.711$ nm
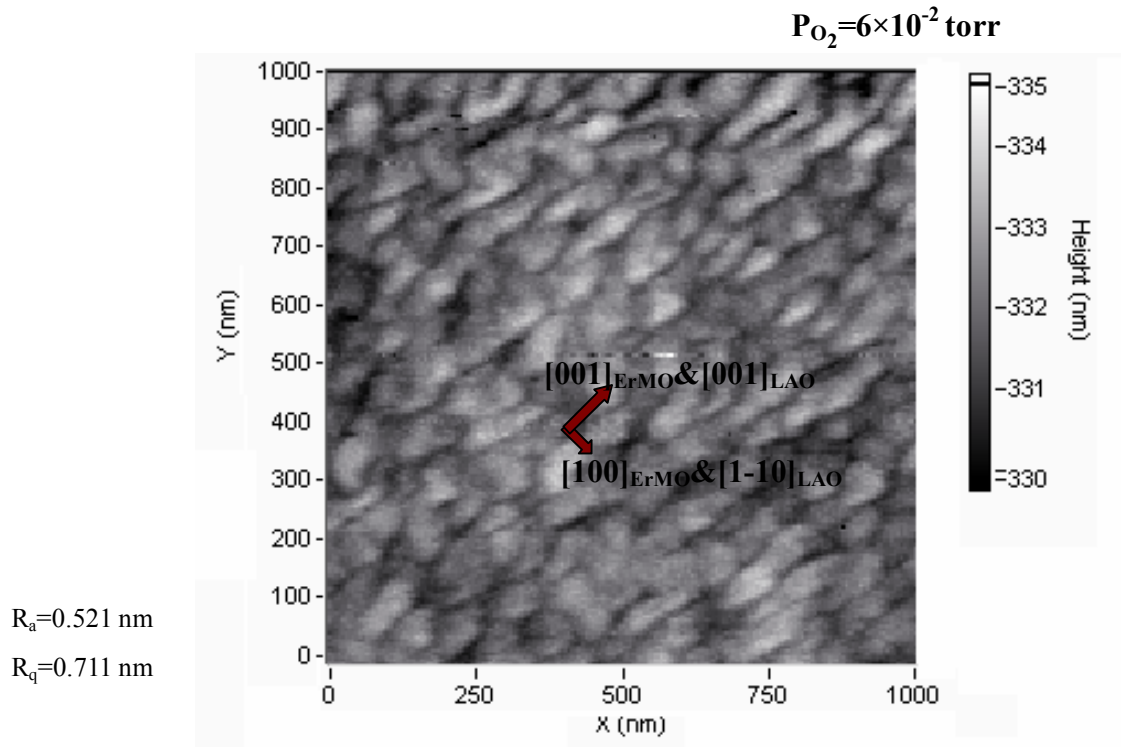
Fig. 4.8 The AFM image of o-ErMO/LAO thin film deposited at $P_{O_2}=6\times10^{-2}$ torr. The arrows

indicate the growth direction of grain.

Table 4.2 The optimized thin film deposition conditions were settled at substrate temperature

880℃ with $P_{O_2}=0.06$ torr. The fitting parameters and in-plane mismatch between o-ErMO

thin film and substrate were listed as follows:

	a (Å)	b (Å)	c (Å)	V (Å³)
o-ErMnO3on LAO(110)	5.25	5.78	7.45	227.37
Powder	5.23	5.80	7.34	222.70
LAO(110) substrate	5.35		7.56	
in-plane mismatch with substrate	2.23%		3.04%	
strain factor	0.44%	-0.36%	2.02%	2.10%

Comparing to lattice constants reported for the o-ErMO powders with a =5.23 Å, b=5.80 Å, and c=7.34 Å, the obtained lattice constants a =5.25 Å, b=5.78 Å, and c=7.49 Å for the present o-ErMO/LAO(110) films evidently indicated an in-plane stretch along the a- and c-axis. This is not surprising considering that the thickness of the films was about 130 nm as derived from the periodicity of Kiessig fringe from X-ray reflectivity measurement.
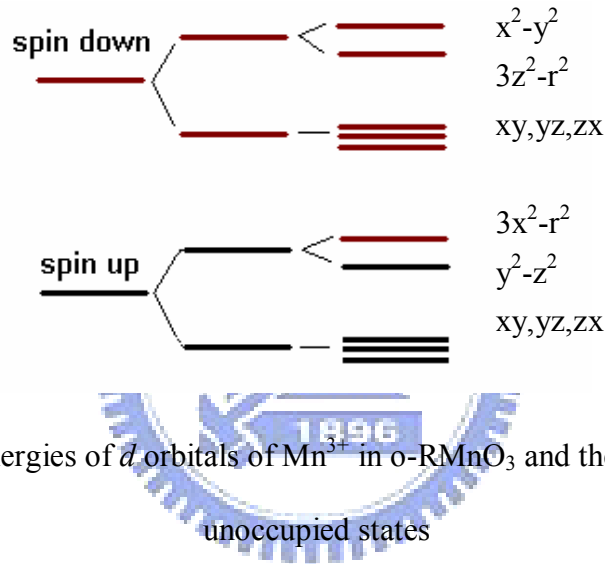
Fig.4.9 Split energies of d orbitals of Mn^{3+} in o-RMnO$_3$ and the red rows represent the unoccupied states

Next, we discuss the electronic structure of the epitaxially-stabilized o-ErMO films. In manganites, the energy levels split into two symmetry groups (e_g and t_{rg}) as a result of crystal field and then the degeneracy of symmetry group is broken again due to Jahn-Teller Effect. As the theoretical calculation and XAS spectra in TbMnO$_3$ and DyMnO$_3$ revealed, the energy level would display as Fig. 4.9 for consideration to the in-plane strong bonding anisotropy. Additionally, according to the results reported by Chen *et al.* [35], the spectra could be divided to three parts. For energy lower than 532.5 eV the absorption spectrum is attributed to

the hybridization of O $2p$ and Mn $3d$ states. On the other hand the feature near 535 eV is due

to O $2p$ states hybridized with Er $5d$ states and the final feature near 542 eV is ascribed to a

band mixed with Mn $4sp$ and Er $6s$ states. Here, we will only focus our attention on the region

of O $2p$ states hybridized with Mn $3d$ states, which is believed to be more relevant to the

magnetic orderings and associated magnetoelectric effects. As shown in Fig. 4.10, the

corresponding features could be represented as $e_{g\uparrow}(d_{3x^2-r^2})$, $t_{2g\downarrow}(d_{xy,yz,xz})$, $e_{g\downarrow}(d_{3z^2-r^2})$ and e_g

$_\downarrow(d_{x^2-y^2})$, which are associated with transitions from the O $1s$ core level into empty O $2p$ states

induced by hybridization with unoccupied majority-spin bands of Mn. The fact that the XAS

spectra display marked anisotropy when probed along respective crystalline axis further

indicate that the structure of ErMnO$_3$ indeed orthorhombic and the crystalline axes of these

o-ErMO are aligned with the substrate very well.
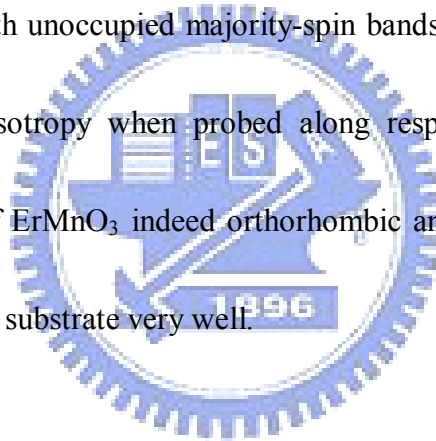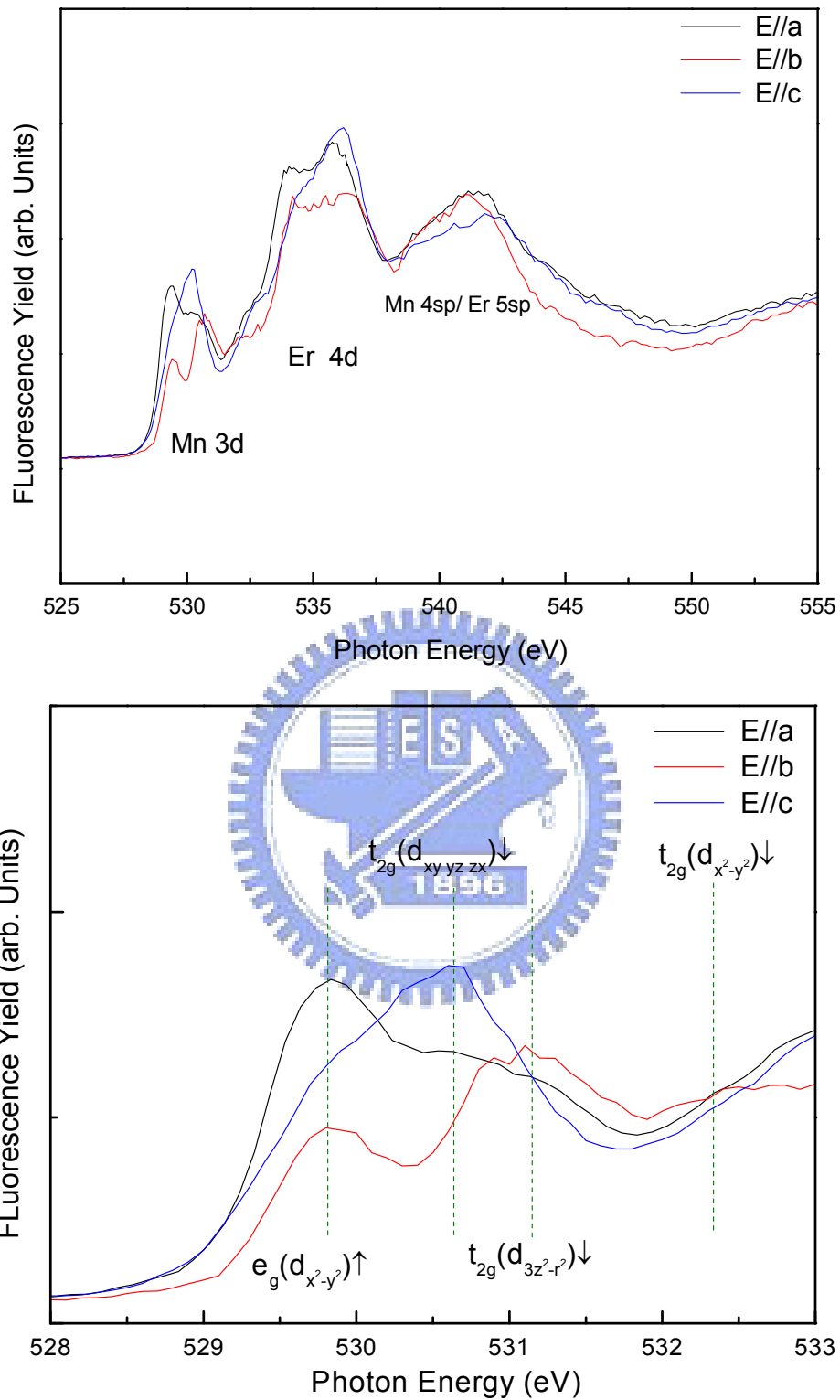
Fig. 4.10 The polarization-dependent O K-edge XAS spectra of o-ErMO/LAO(110) deposited

at $P_{O_2}=6\times10^{-2}$ torr thin film recorded at room temperature for three different polarizations:

E//*a*-axis, **E**//*b*-axis, and **E**//*c*-axis
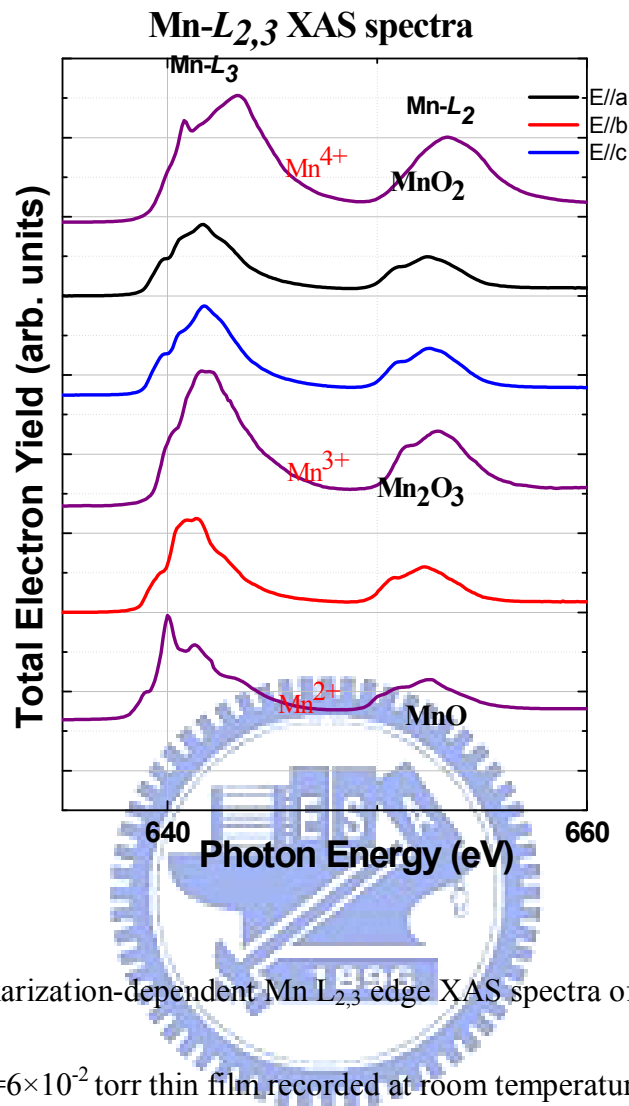
Mn-$L_{2,3}$ XAS spectra

Fig. 4.11 The polarization-dependent Mn $L_{2,3}$ edge XAS spectra of o-ErMO/LAO(110

deposited at $P_{O_2}=6\times10^{-2}$ torr thin film recorded at room temperature for three different

polarizations: **E**//a-axis, **E**//b-axis, and **E**//c-axis

Fig. 4.11 shows polarization-dependent Mn $L_{2,3}$ edge absorption spectra of o-

ErMO/LAO thin film collected with **E**//a, **E**//b, and **E**//c and that of standard MnO, Mn_2O_3,

and MnO_4 powders. There was only slight difference in Mn L_2 peak for electric field applying

along various directions, while the shape of Mn L_3 peak for **E**//b was more similar to trivalent

manganese, indicating that the ionic valence of Mn spin in o-ErMO was trivalent and its

projection on b-axis was more than on other directions. Although there was no neutron

diffraction data to illustrate the magnetic structure of o-ErMO, it was well established that the

Mn^{3+} spins in o-HoMO and o-YMO aligned in *b*-axis by neutron diffraction measurement.

Thus, more projection on *b*-axis could be understood. Besides, the main Mn $L_{2,3}$ peaks for

E//*b* polarization in XAS spectra of o-ErMO/LAO lies at a lower energy than for polarizations

E//*a* and **E**//*c*. The diverseness in spectra for these polarizations shows a great anisotropy in

Mn *3d*-O-*2p* hybridization, which is consistent with the results of O K-edge absorption

spectra in Fig. 4.10.

$P_{O_2}=6\times10^{-2}$ torr
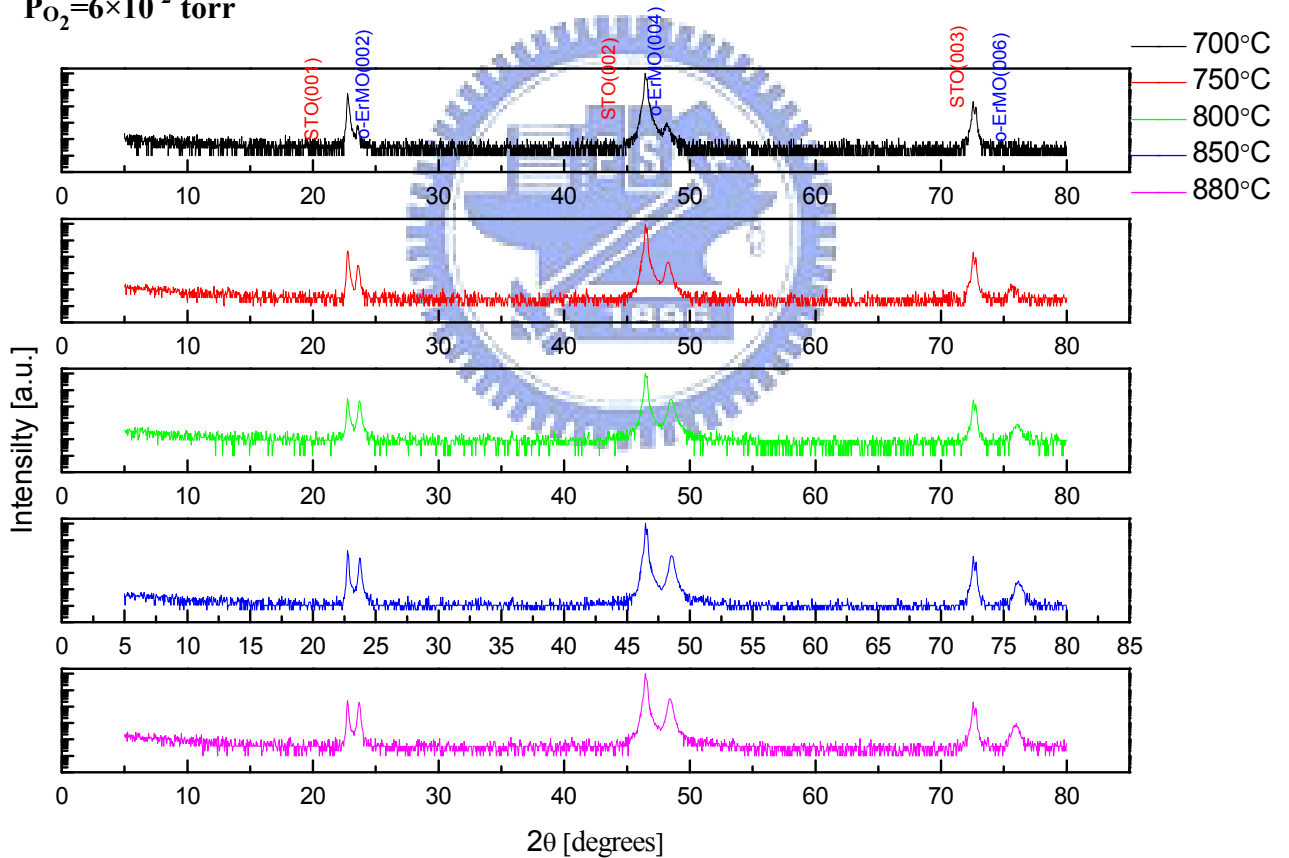
Fig. 4.12 XRD patterns of o-ErMO/STO(001) deposited at different substrate temperatures

In addition to depositing on LAO (110) substrates, we have also tried to grow o-ErMO

films on $SrTiO_3$ (001) [STO (001)] at different substrate temperatures. Since the intensity of

o-ErMO (00l) increases with increasing substrate temperature, we chose 880℃ and 6×10^{-2}

torr as the optimal deposition conditions (Fig. 4.12). The XRD data evidently confirmed the

formation of pure o-ErMO with c-axis oriented normal to the film surface; nevertheless, a and

b lattice constants are so similar that they randomly grown on the diagonal lines of STO (001).

As sown in Fig. 4.13, the phi scan displayed two pairs of twofold symmetry attributed the

in-plane a- and b-axis mixing mosaic alignment with substrate while keep the c-axis

orientation intact. This is, presumably, due to the similarity between the a- and b-axis lattice

constants. The circular grains of o-ErMO/STO(001) displayed in the AFM image (Fig. 4.15),

indeed, are not as anisotropic as those seen in o-ErMO/LAO(110) films.

Fig. 4.13 The φ-scans of the o-ErMO/STO(001) thin film deposited at P_{O_2}=6×10^{-2} torr and
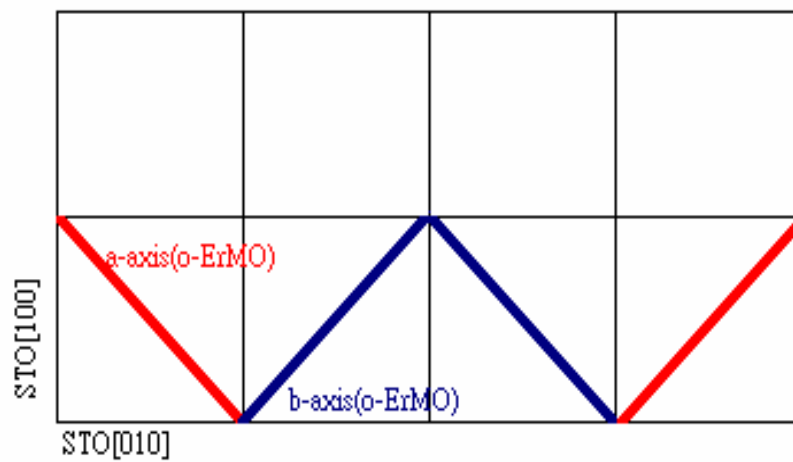
T_s=880℃

Fig. 4.14 In-plan arrangements between the o-ErMO thin films and STO(001) substrate

R_a=0.833 nm
R_q=1.066 nm

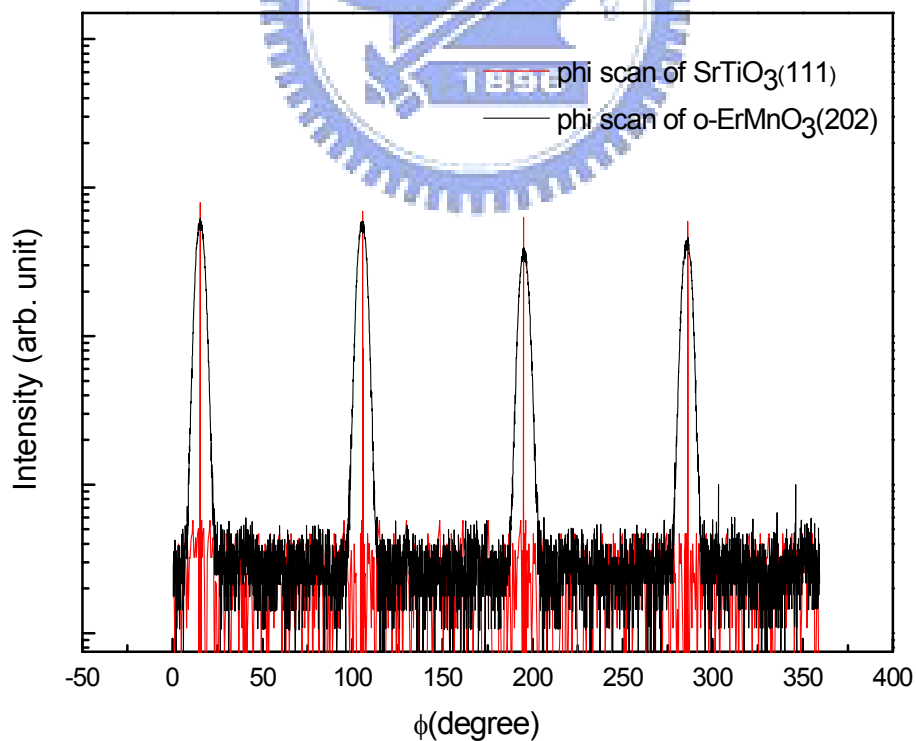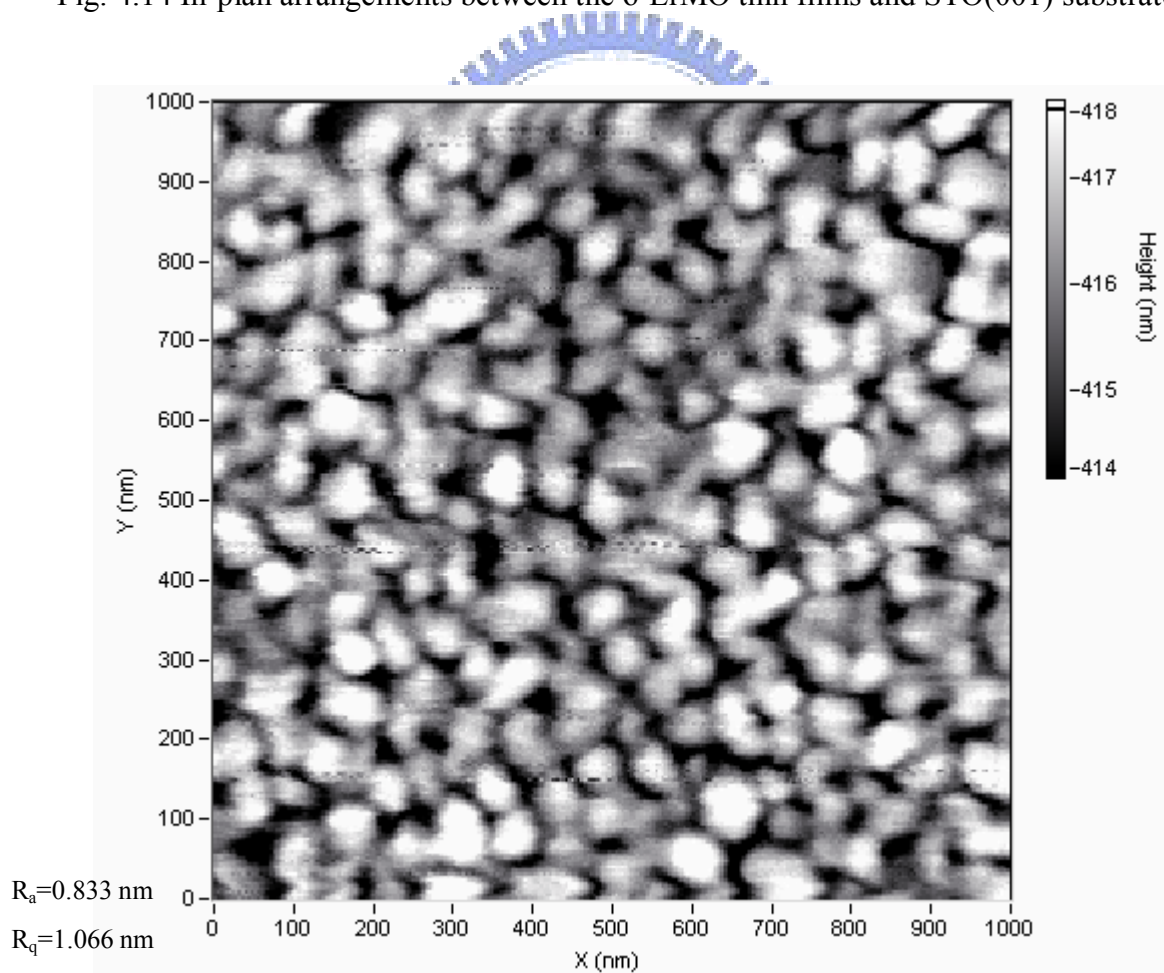Fig. 4.15 The AFM image of o-ErMO/STO(001) thin film deposited at P_{O_2}=6×10^{-2} torr and

T$_s$=880℃.

4.2.2 The magnetic properties

Fig. 4.16 shows the temperature dependent magnetization $M(T)$ of o-ErMO/LAO(110) measured by the zero-field-cooled (ZFC) scheme with an external field 100 Oe (**H**=100 Oe) applied along three respective crystal orientations. As shown in figure, all ZFC $M(T)$ curves of o-ErMO display an antiferromagnetic transition of Mn moment near 42K, which is consistent with previous results [11,18]. Another transition in magnetic ordering from Er^{3+} is clearly seen around 3.5K, in which antiferromagnetic ordering measured with **H**//c-axis is different from ferromagnetic ordering with **H**//b-axis. Last of all, both the ZFC $M(T)$ probed with **H**//c-axis and the inverse susceptibility $\chi^{-1}(T)$ probed with **H**//a-axis and **H**//b-axis (Fig. 4.17) display a transition near 18K, presumably due to spin reorientation (T_{SR}) of Mn moment.
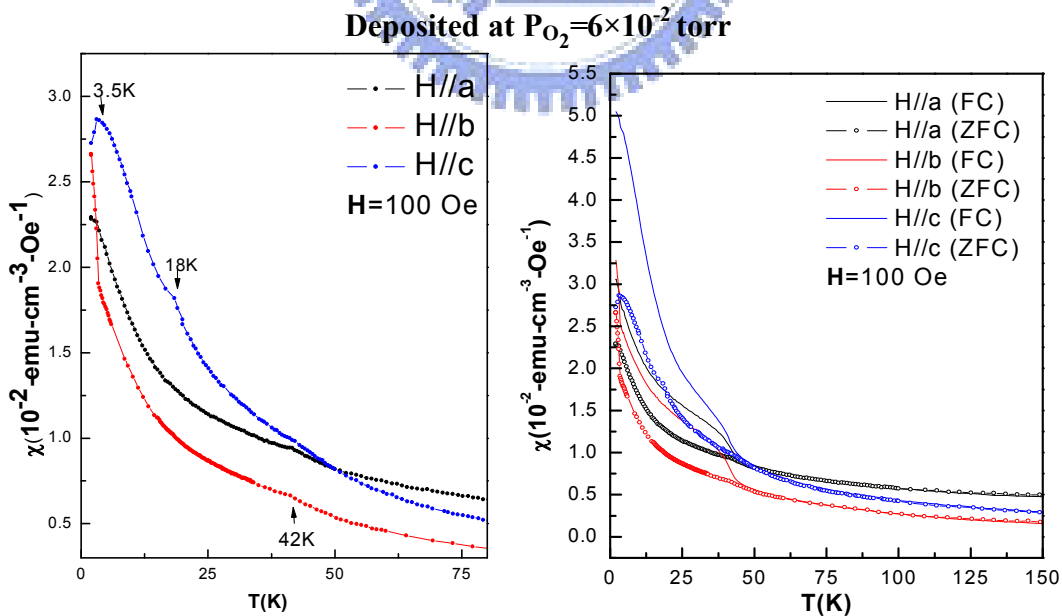
Fig. 4.16 The temperature dependent magnetization of o-ErMO/LAO(110) with external field applied along respective crystal orientation
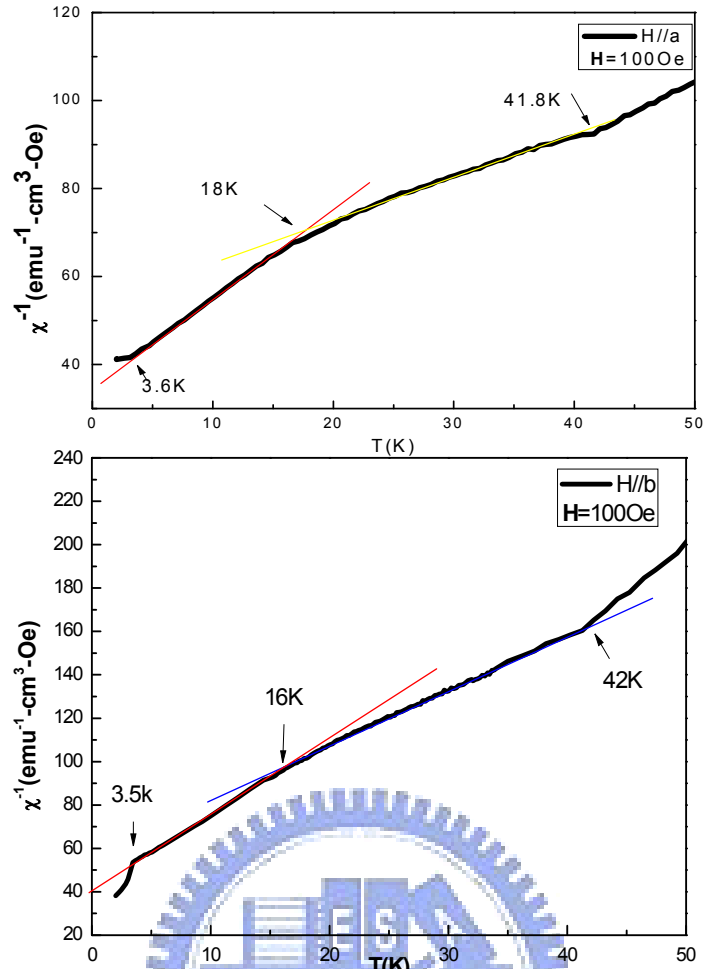
Fig. 4.17 The inverse susceptibility $\chi^{-1}(T)$ probed for **H**//a-axis and **H**//b-axis display a

transition near 18K

However, as shown in Fig. 4.18, ZFC *M(T)* of o-ErMO/STO(001) probed with **H**=100

Oe applied parallel and perpendicular to plane exhibited somewhat different from that of

o-ErMO/LAO(110). When the field was applied along the *c*-axis of *o*-ErMO/STO(001), the

anomalies in *M(T)* were observed at 44, 28 and 3.5K, probably attributed to antiferromagnetic

transition and T_{SR} of Mn moments and Er^{3+} ordering, respectively. In comparison, when the

field was applied along the *ab*-plane of *o*-ErMO/STO(001), there is no transition could be

unambiguous identified.
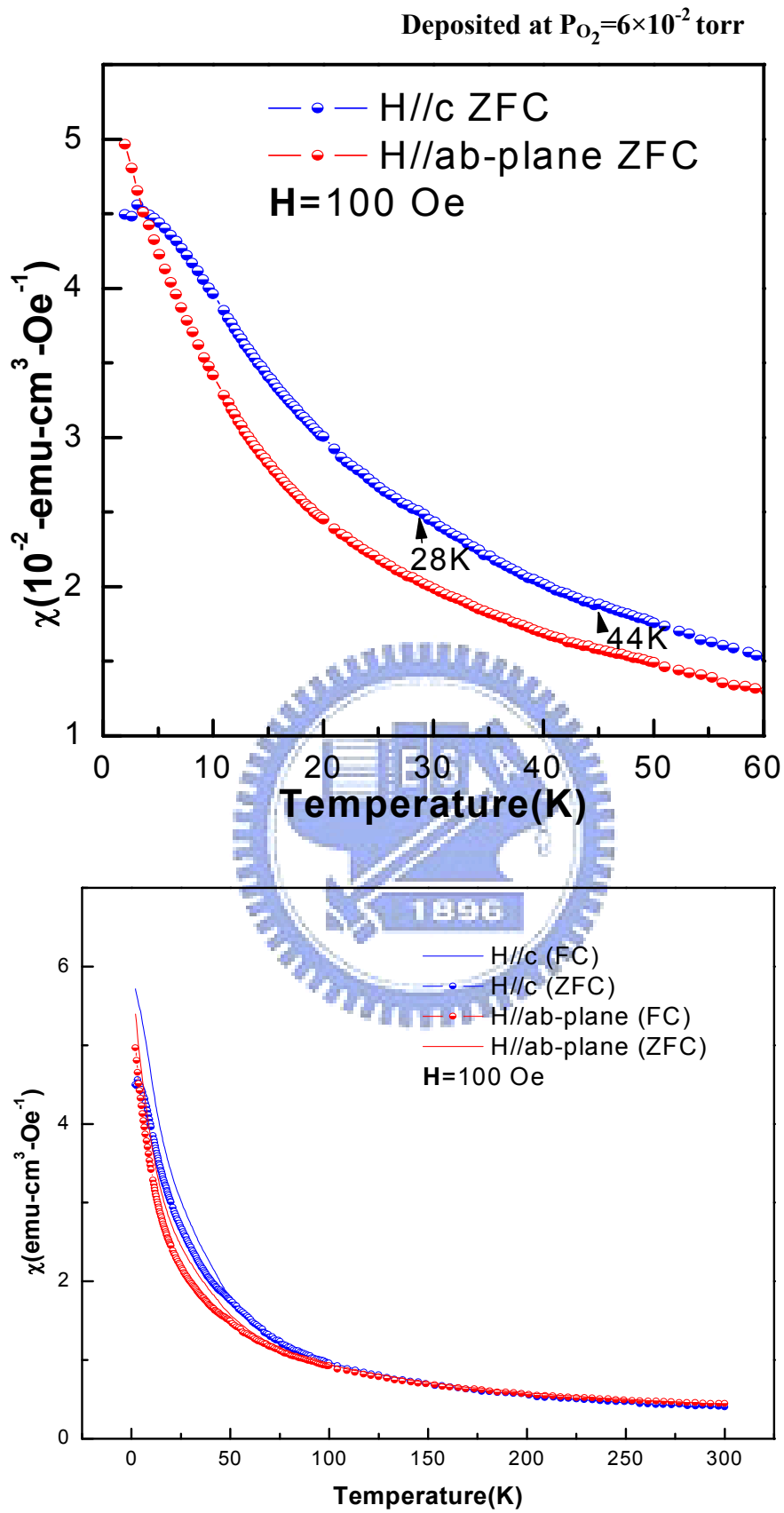
Fig. 4.18 The temperature dependent magnetization of o-ErMO/STO(001) with the external

field applied parallel and perpendicular to film plane
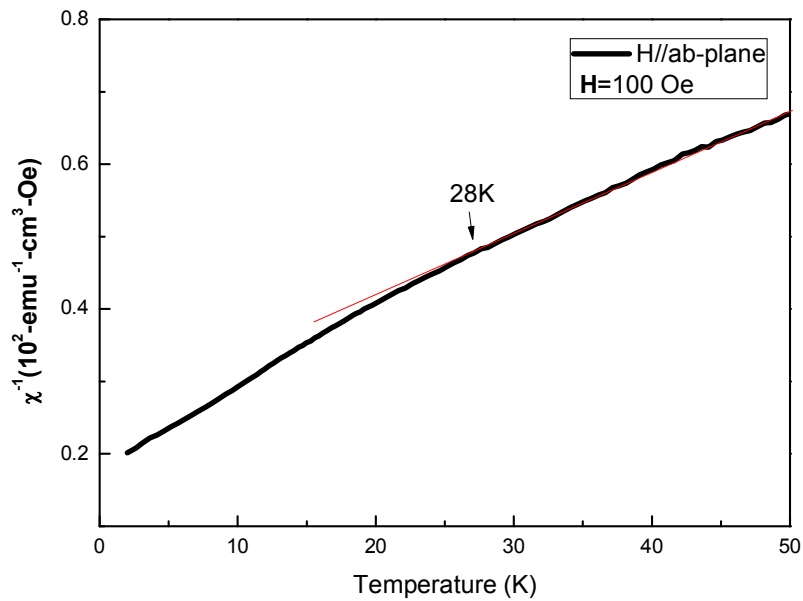
Fig. 4.19 The inverse susceptibility $\chi^{-1}(T)$ probed for H//*ab*-plane display two transition near

45K and 28K

Spin reorientation of Mn moment

Three distinctive magnetic transitions were observed for o-ErMO films grown on both

LAO and STO substrates (Fig. 4.18). The first one locating around 42K is apparently

associated to the antiferromagnetic ordering of Mn moment and, thus, it is assigned as the

Neel temperature (T_N). The second transition was observed near 18K for o-ErMO/LAO(110),

which is markedly different from the transition at 28K for o-ErMO/STO(001). The last

transition was dominated by the moments from erbium ions at lower temperatures. The two

AFM transitions of Mn^{3+} and Er^{3+} moments appear to be rather insensitive to the substrates on

which the films were grown. However, there is a 10-Kelvin difference in the spin

reorientation transition identified for the Mn-moment when different substrates were used.

This discrepancy seems to be more relevant to the strain arising from film/substrate epitaxy.

In order to understand this intriguing observation, we first ask what the possible origin of the T_{SR} is. The lock-in transition could be one source of T_{SR}. The wave vector (0, k_b, 0) of the AFM ordering of the Mn moment is with $k_b \approx 0.415$ for temperature immediately below T_N. K_b gradually increasing with decreasing temperature and locks into a temperature independent constant 0.433 at 28K, which was called the lock-in temperature (T_L) [18]. The 28-Kelvin transition was also seen in temperature dependent dielectric constant ε (T) and specific heat C_p(T) [11]. However, since lock-in transition was primarily involved with the periodicity of magnetic ordering and that of underlying lattice, thus it seldom displays a marked manifestation in *M(T)* measurements previously. The recent investigations performed on strain-stabilized films, on the other hand, not only have clearly revealed the lock-in transition in the *M(T)* measurement but also have implied the prominent also played by the strain in the magnetic behavior and associated ferroelectricity [7, 8, 37, 38]. The influence of strain on Mn-O-Mn bonds presumably is the primary reason in modifying the magnetic properties.

With this in mind, we tried to compare the *M(T)* curves for films grown on these two different substrates. The *M(T)* of o-ErMO/LAO(110) shows a marked hysteresis in ZFC-FC data as compared with that of o-ErMO/STO(001). One of the possible origins of this irreversibility might have resulted from the spin-glass behavior. It could be also due to magnetic canting and uncompensated spins of structural origin. Although the susceptibility measurement might be not enough to unravel the origin of this magnetic hysteresis, the

comparison is, nevertheless, indicating that the spins in o-ErMO/LAO(110) are more disorder than that in o-ErMO/STO(001).

Finally, we notice that since for o-ErMO/STO(001) the *a*- and *b*-axis of the film crystalline orientation is mixed in-plane, the resultant *M(T)* when measured with field applied in plane is indeed displaying characteristics consistent with that reported for o-ErMO powder. The fact that no T_{SR} was seen in polycrystals and powders of o-RMnO$_3$ (R=Y,Ho-Lu) and even T_N only could be seen in the compounds (YMnO, LuMnO) where the rare earth does not contribute any magnetic moment [3, 18, 38, 39]. It indicates that although the transition of Mn moments in *M(T)* is easily overwhelmed by the paramagnetic signal of the rare earth moments. As a result, it can not be revealed easily in *M(T)*. The present results, however, suggest that epitaxial might be helpful to display the transition of Mn moments.

The magnetic ordering for the Er^{3+} moments

After discussing the magnetic properties of T_{SR}, we also want to comprehend the feature of Er^{3+}. As shown in Fig. 4.16 and Fig. 4.18, the ordering of Er^{3+} moments is clearly seen around 3.5K, in which antiferromagnetic ordering measured with **H**//*c*-axis is different from ferromagnetic ordering with **H**//*b*-axis. It seems reasonable to conjecture that the spins of Er^{3+} were antiferromagnetic arrangement along *c* axis and leaned toward *b*-axis. Although not perceived in the *M(T)* of o-ErMO due to mixture of data with three distinct crystal orientations, this transition of Er^{3+} was observed for hexagonal ErMnO$_3$ single crystal [33].

Moreover, when the field was applied along *c*-axis, the typical characteristic of antiferromagnetism also revealed by the looking at variation in slope at different temperatures in the field dependent magnetization *M(H)* (Fig. 4.20). Nevertheless, an obvious hysteresis at low temperature is observed in the *M(H)* curves, indicative of noncollinear orderings, similar to that seen in o-HoMnO₃ polycrystals [3].
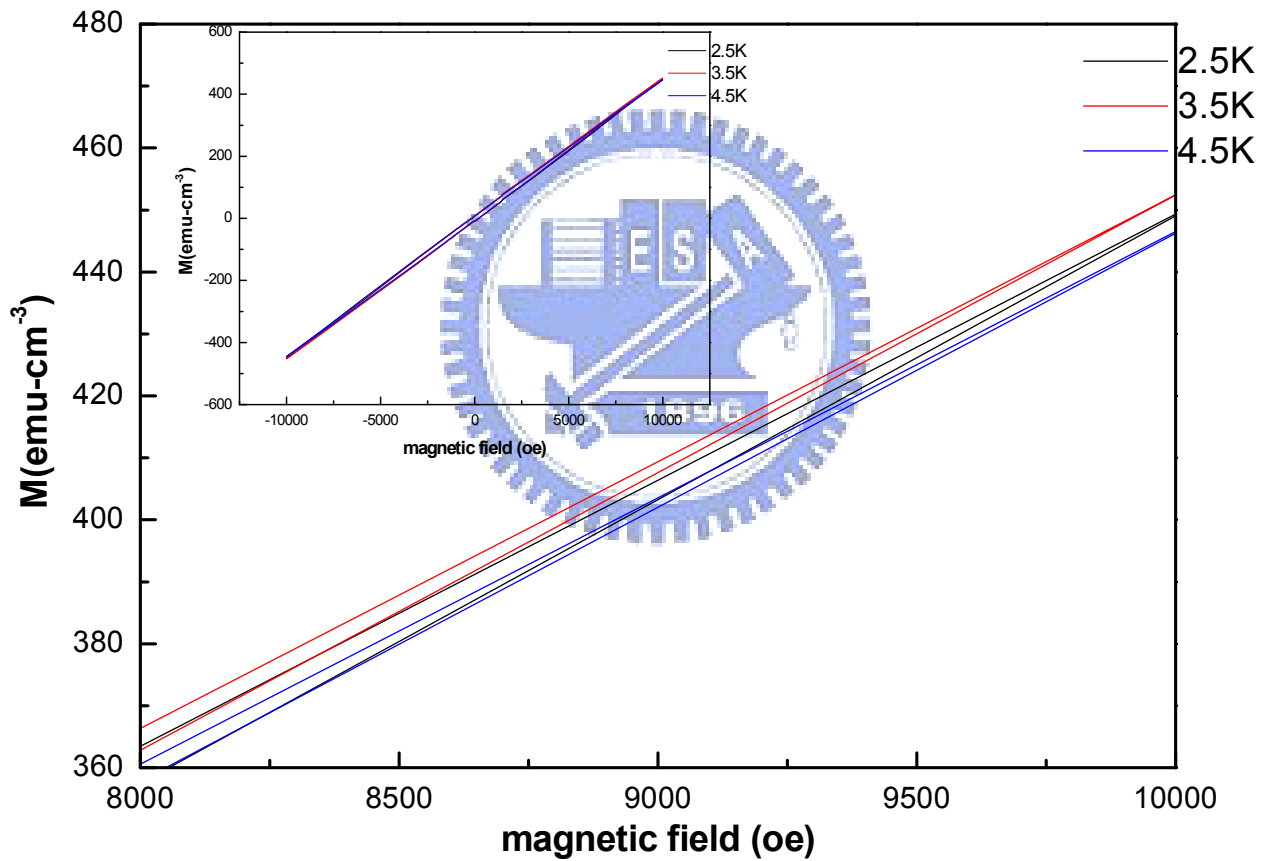

Fig. 4.20 The field dependent magnetization with **H**//*c* at different fixed temperature for o-ErMnO/STO(001) deposited at $P_{O_2}=6\times10^{-2}$ torr
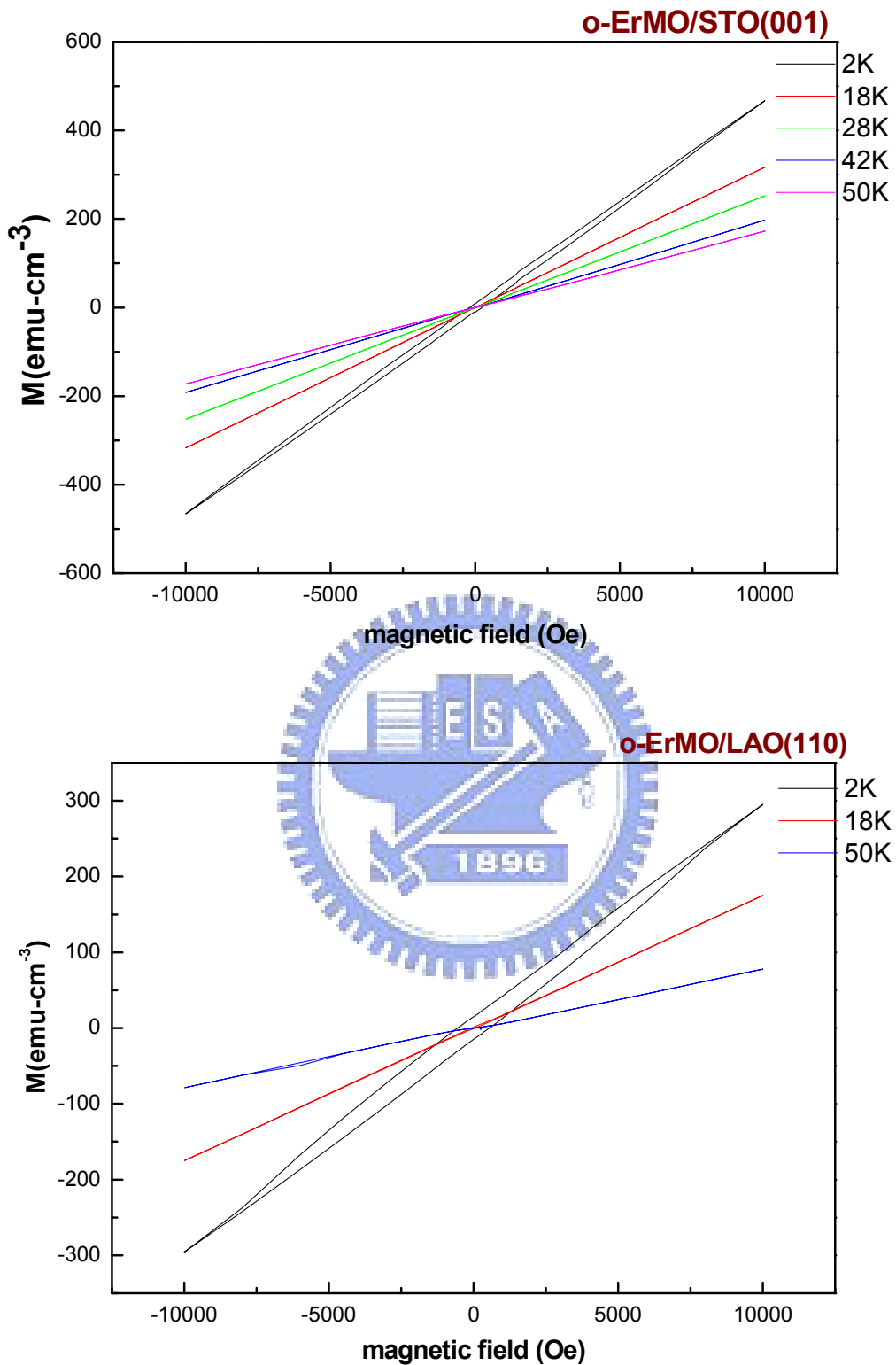
Fig. 4.21 The field dependent magnetization with **H**//*c* at different fixed temperature

The hysteresis only appears at low temperatures, suggesting that it results from the

ordering of Er^{3+}.

The magnetic structure of o-ErMO is a contention

The magnetic structure of o-ErMO is controversial at present. Although the magnetic structure for o-ErMO has not yet been studied in detail, the continuous evolution in T_{SR} from R=Ho to Lu through heat capacity measurements strongly suggests that the nature of the spin structure does not change in R=Ho-Lu [11] and the magnetic structure of o-ErMO was assumed to be the E-type in recent researches [40 , 41]. However, the magnetic structure of o-ErMO was determined to be incommensurate (ICM) below T_L with a fixed propagation vector q = (0, 0.433, 0), in contrast to the generally accepted E-type, and its magnetic modulation is closely resemble to that of o-YMO, in which the ICM locks onto a wave vector (0, 0.435, 0). Thus, Ye *et al.* argued that the magnetic structure of o-ErMnO$_3$ is not E-type but is similar to that of o-YMO which is believed to have helix characteristic [18]. In this study, we found that o-ErMO and o-YMO have the same tendency on *M(T)*. As shown in Fig. 4.22, the magnitude of o-ErMO susceptibility for **H**//*a* is higher than that for **H**//*b* and the highest susceptibility is observed for **H**//*c*. It is interesting to note that the ordering is similar to that exhibited in o-YMO films [7], however, is different from that of o-HoMO [6]. The magnetic anisotropy for the rare-earth moments is also displaying very different behaviors for o-ErMO and o-HoMO. In addition to the comparisons made on *M(T)*, o-ErMO and o-YMO, nevertheless, exhibited very similar results in neutron powder diffraction pattern and temperature dependent dielectric constant ε (T) [12, 13, 18].
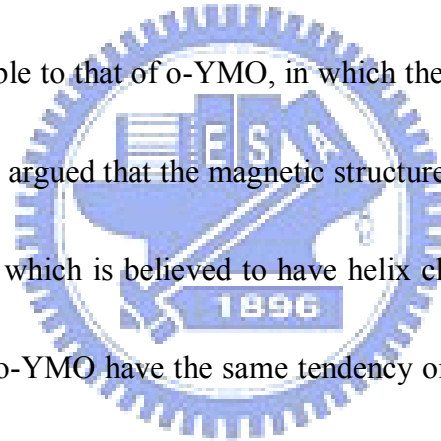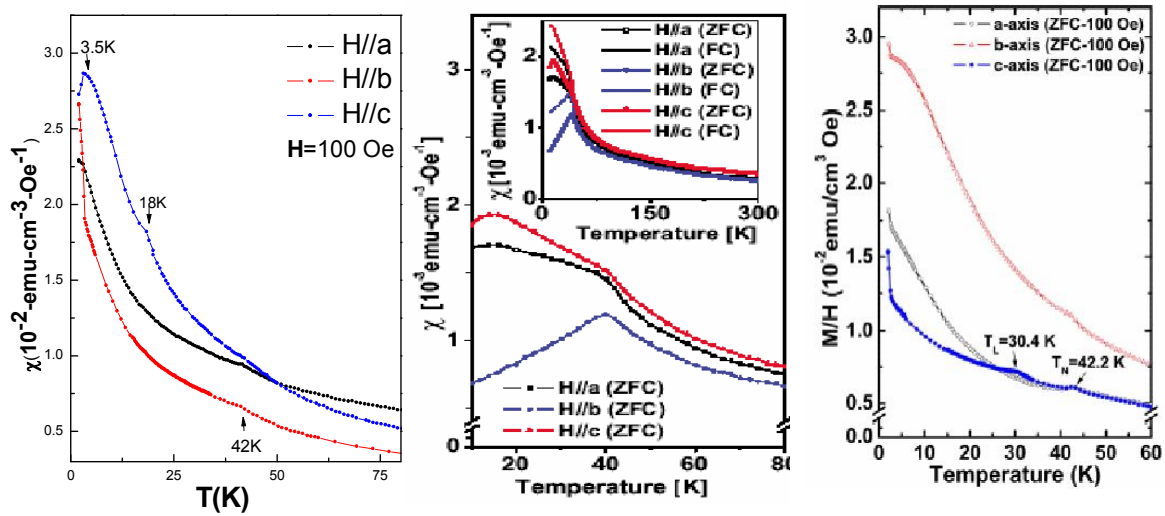
Fig. 4.22 Comparing the magnetization of o-ErMO/LAO(110) with that of o-YMnO₃ and o-HoMnO₃ [6, 7]

4.3 The effect of low oxygen pressure during deposition

As mentioned above, the films deposited in low P_{O_2} circumstance would cause twin-like structure, so we also want to discuss the effect of low P_{O_2} on the magnetic structure in this section. As shown in Fig. 4.24, the ZFC and FC for sample deposited at $P_{O_2}= 6\times10^{-4}$ torr begin to separate from each other below 90K and 84K, while the ZFC curves display peaks around 72K and 66K for **H**//out-of-plane and **H**//in-plane, respectively. The anisotropic magnitude tendency for $P_{O_2}= 6\times10^{-4}$ torr (out of plane $\approx$ in plane) was also different from that for $P_{O_2}=6\times10^{-2}$ torr ($c>a>b$). In addition, the transition of Er^{3+} disappears and the *M(H)* curve exhibits a hysteresis at 50K (Fig. 4. 23). These features may be more relevant to spin glass (SG) [42, 43], which are not seen in the films deposited at $P_{O_2}=6\times10^{-2}$ torr and 6×10^{-3} torr. As revealed in Fig. 4.4, the o-ErMO (020) peaks for $P_{O_2}=6\times10^{-3}$ torr and 6×10^{-4} torr locate at the same 2θ angle,

52

thus the strain in the films appears not being drastically different. However, neither *M(T)* nor

M(H) for 6×10^{-3} torr depicted any characteristic of SG behavior, which implies that oxygen

defect rather than strain might be the main source of SG. for the films deposited in $P_{O_2}=6\times10^{-4}$.

Oxygen loss may cause more Mn^{2+} states to form or structure defect to induce SG. If Mn^{2+}

states increase, it will enhance the double exchange interaction between Mn^{2+} and Mn^{3+} to

promote the ferromagnetic interaction, which in turn competes with antiferromagnetic

interaction and results in SG.
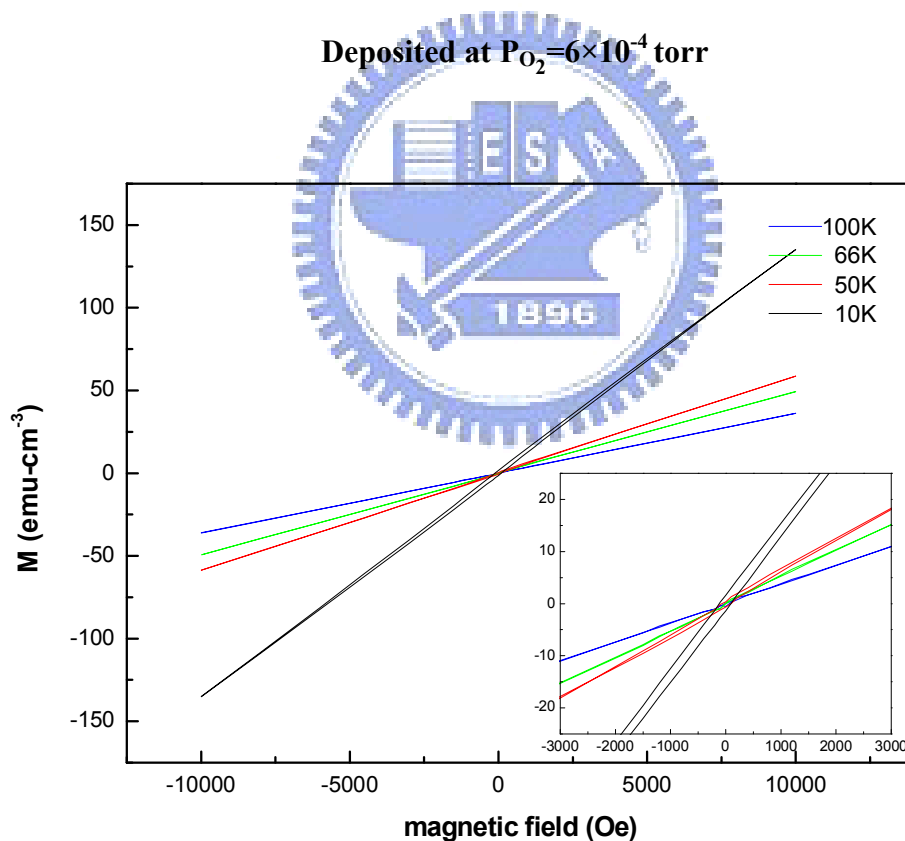

Fig. 4.23 The field dependent magnetization with **H**//*c* at different fixed temperature

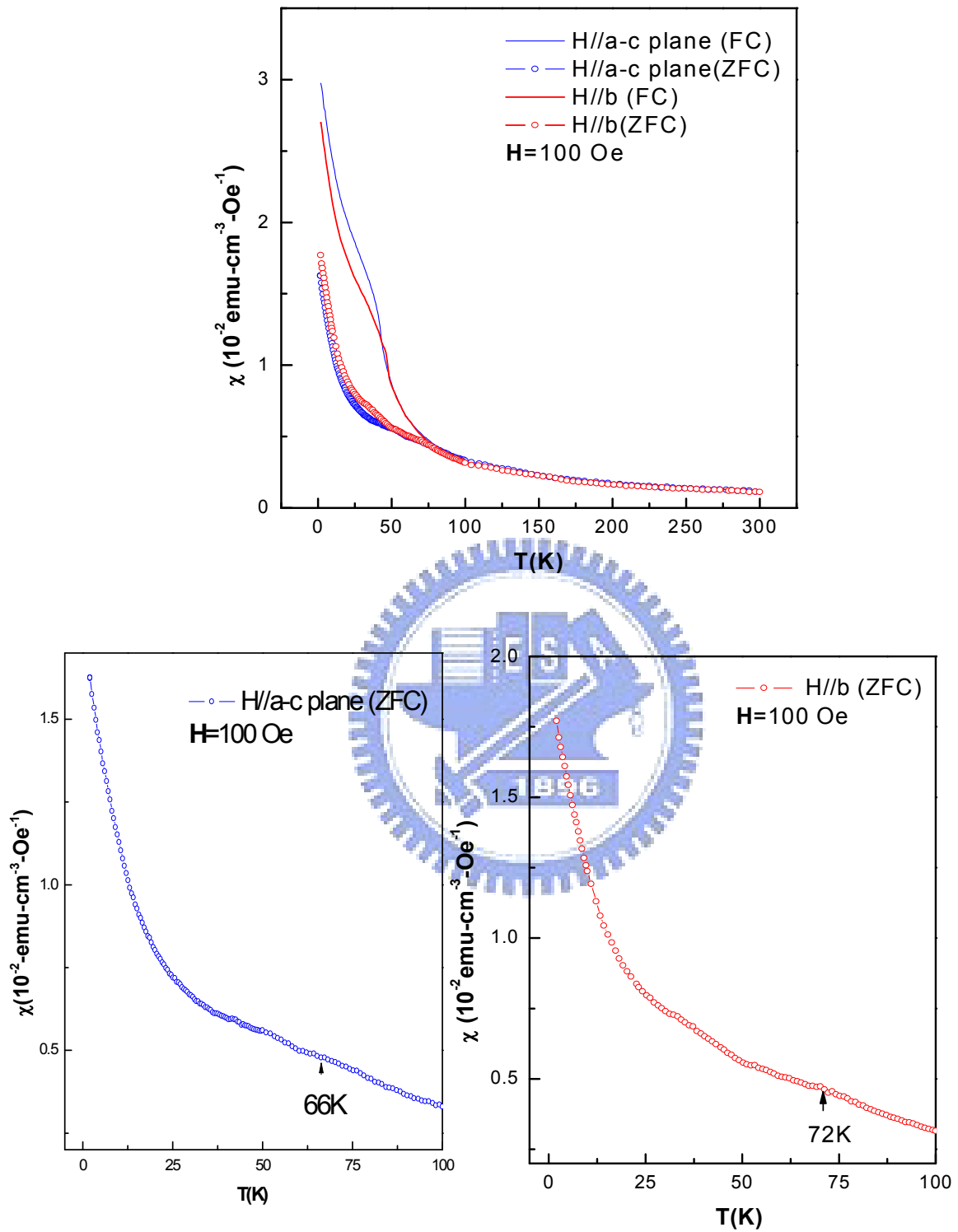The hysteresis showed at 50K, indicating that the feature may be more relevant to spin glass.

Fig. 4.24 ZFC and FC *M(T)* of o-ErMO/LAO(110) deposited at $P_{O_2}=6\times10^{-4}$ torr with external

field applied parallel and perpendicular to plane

Chap.5 Summary

The b-axis and c-axis oriented o-ErMO films are successfully grown on LAO(110) and STO(001) by PLD, respectively. XAS spectra allowed us to conform that the structure of ErMnO$_3$ was orthorhombic and that the projection of Mn^{3+} spin in the b-axis is more than that in other directions. Furthermore, these o-ErMO films provided the possibility for probing anisotropic magnetization. Three magnetization anomalies were seen for films deposited on both substrates, with the well-characterized AFM transition for Mn moments around 42K and the AFM transition of Er^{3+} at 3.5K. However, there is a 10-Kelvin difference in the temperature of the second transitions for the films deposited on the two different substrates. The high-order moments laying on o-ErMO/STO(001) exhibited T$_{SR}$ at 28K, which coincided with T$_L$, whereas the T$_{SR}$ for o-ErMO/LAO(110) is around 18K. The difference is presumably due to the strain state established during deposition. On the other hand, in addition to exhibiting a twin-like structure, the o-ErMO/LAO(110) films deposited at lower oxygen pressure also showed the existence of spin glass phase. The magnetic results of the present study need to be compared with electric properties to delineate how the two are coupling to each other.
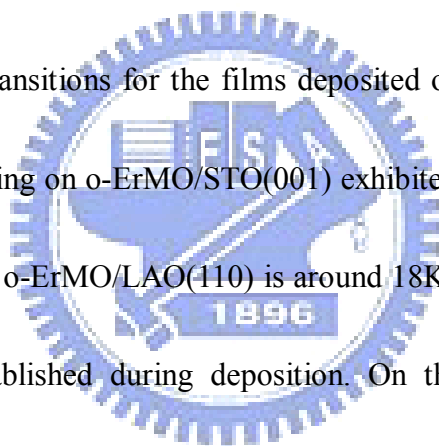
Reference

[1] T. Kimura, T. Goto, H. Shintani, K. Ishizaka, T. Arima, Y. Tokura, Nature. 426 55-58. (2003)

[2] B. Lorenz, Y.Q. Wang, C.W. Chu, Physical Review B. 76 104405 (2007)

[3] B. Lorenz, Y.Q. Wang, Y.Y. Sun, C.W. Chu, Physical Review B. 70 212412 (2004)

[4] N.A. Hill, The Journal of Physical Chemistry B. 104 6694-6709 (2000)

[5] S.W. Cheong, M. Mostovoy, Nature Materials. 6 13-20 (2007)

[6] T.H. Lin, C.C. Hsieh, H.C. Shih, C.W. Luo, T.M. Uen, K.H. Wu, J.Y. Juang, J.-Y. Lin, C.-H. Hsu, S.J. Liu, Applied Physics Letters. 92 132503 (2008)

[7] C.C. Hsieh, T.H. Lin, H.C. Shih, C.-H. Hsu, C.W. Luo, J-Y. Lin, K.H. Wu, T. M. Uen, J.Y. Juang, Journal of Applied Physics. 104 103912 (2008)

[8] T.H. Lin, H.C. Shih, C.C. Hsieh, C.W. Luo, J.-Y. Lin, J. L. Her, H. D. Yang, C.-H. Hsu, K.H. Wu, T. M. Uen, J.Y. Juang, Jourmal of Physics: Condensed Matter. 21 026013 (2009)

[9] W. Prellier, M.P. Singh, P. Murugavel, Journal of Physics-Condensed Matter. 17 R803-R832 (2005)

[10] K. Uusi-Esko, J. Malmb, N. Imamura, H. Yamauchi, M. Karppinen, Materials Chemistry and Physics. 112 1029–1034 (2008)

[11] M. Tachibana, T. Shimoyama, H. Kawaji, T. Atake, E. Takayama-Muromachi, Physical

Review B. 75 144425 (2007)

[12] A. Munoz, J.A. Alonso, M.T. Casais, M.J. Martinez-Lope, J.L. Martinez, M.T. Fernandez-Diaz, Journal of Physics-Condensed Matter. 14 3285-3294 (2002)

[13] J.A. Alonso, M.J. Martinez-Lope, M.T. Casais, Inorganic Chemistry. 39 917-923 (2000)

[14] T. Kimura, G. Lawes, T. Goto, Y. Tokura, A.P. Ramirez, Physical Review B. 71 224425 (2005)

[15] I.A. Sergienko, C. Sen, E. Dagotto, Physical Review Letters. 97 227204 (2006)

[16] S. Picozzi, K. Yamauchi, B. Sanyal, I.A. Sergienko, E. Dagotto3, Physical Review Letters. 99 227201(2007)

[17] T. Goto, T. Kimura, G. Lawes, A. P. Ramirez, Y. Tokura,, Physical Review Letters. 92 257201 (2004)

[18] F. Ye, B. Lorenz, Q. Huang, Y.Q. Wang, Y.Y. Sun, C.W. Chu, J.A. Fernandez-Baca, Pengcheng Dai, H.A. Mook, Physical Review B. 76 060402 (2007)

[19] R.L. Comstock, Introduction to magnetism and magnetic recording, John Wiley & Sons, New York, (1999).

[20] C. Zener, Physical Review. 82 403 (1951)

[21] P.W. Anderson, H Hasegawa, Physical Review. 100 675 (1955)

[22] Y. Tokura, N. Nagaosa, Science. 288 462-468 (2000)

[23] M. Gerloch, R.C. Slade, Ligand-Field Parameters, Cambridge, London, (1973).

[24] H. Jahn, E. Teller, Physical Review. 49 874 (1936)

[25] R, Janes, E.A. Moore, Metal-ligand bonding, Royal Society of Chemistry, (2004)

[26] R. Kajimoto, H. Mochizuki, H. Yoshizawa, H. Shintani, T. Kimura, Y. Tokura, Journal

of the Physical Society of Japan. 74 September 2430–2433 (2005)

[27] G. Maris, V Volotchaev, T.T.M Palstra, New Journal of Physics. 6 153 (2004)

[28] D. Khomskii, Physics. 2 20 (2009)

[29] M. Mostovoy, Nature Materials. 7 269 – 270 (2008)

[30] D.B. Chrisey and G.K. Hubler, Pulsed laser deposition of thin films, John Wiley &

Sons, New York, (1994).

[31] S.L. Morelhao, Journal of Synchrotron Radiation. 10 236241 (2003)

[32] R.L. Fagaly, Review of Scientific Instruments. 77 101101 (2006)

[33] N. Iwata, K. Kohn, Ferroelectrics. 219 1 November 161 – 168 (1998)

[34] K.U. Esko, J. Malmb, N. Imamura, H. Yamauchi, M. Karppinen, Materials Chemistry

and Physics. 112 1029–1034 (2008)

[35] J.M. Chen, J.M. Lee, C.K. Chen, T.L. Chou, K.T. Lu, S.C. Haw, K.S. Liang, C.T. Chen,

H.T. Jeng, S.W. Huang, T.J. Yang, C.C. Shen, R.S. Liu, J.Y. Lin, Z. Hu, Applied Physics

Letters. 94 044105 (2009)

[36] X. Martí, V. Skumryev, V. Laukhin, F. Sánchez, M.V. García-Cuenca, C. Ferrater, M.

Varela, J. Fontcuberta, Journal of Materials Research. 22 8 (2007)

[37] X. Martí, V. Skumryev, A. Cattoni, R. Bertacco, V. Laukhina, C. Ferrater, M.V. Garc-Cuenca, M. Varela, F. Sanchez, J. Fontcuberta. Journal of Magnetism and Magnetic Materials. 321 11 1719-1722 (2009)

[38] V.Y. Pomjakushin, M. Kenzelmann, A. Donni, A.B. Harris, T. Nakajima, S. Mitsuda, M. Tachibana, L. Keller, J. Mesot, H. Kitazawa, E. T. Muromachi arXiv:cond-mat.mtrl-sci. v1 0901.0787 (2009)

[39] H. Okamoto, N. Imamura, B.C. Hauback, M. Karppinen, H. Yamauchi, H. Fjellvag, Solid State Communications. 146 152–156 (2008)

[40] K. Yamauchi, F. Freimuth, S. Blügel, S. Picozzi, Physical Review B 78 (2008) 014403

[41] C.Y. Ren, Physical Review B 79 125113 (2009)

[42] S. Y. Jang, D. Lee, J.H. Lee, T.W. Noh, Y. Jo, M.H. Jung, J.S. Chung3, Applied Physics Letters. 93 162507 (2008)

[43] W.R. Chen, F.C. Zhang, J. Miao, B. Xu, X.L. Dong, L.X. Cao, X.G. Qiu, B.R. Zhao Applied Physics Letters. 87 042508 (2005)